1 **Evaluation of filtering methods for use on high-frequency measurements of**

2 **landslide displacements**

3 Sohrab Sharifi[1], Michael T. Hendry[1], Renato Macciotta[1], Trevor Evans[2]

4 *[1]Department of Civil and Environmental Engineering, University of Alberta, Edmonton, AB,*
5 *Canada*

6 *[2]Canadian National Railway, Kamloops, BC, Canada*

8 **Abstract**

9 Displacement monitoring is a critical control for risks associated with potentially sudden slope

10 failures. Instrument measurements are, however, obscured by the presence of scatter. Data

11 filtering methods aim to reduce the scatter and therefore enhance the performance of early

12 warning systems (EWSs). The effectiveness of EWSs depends on the lag time between the onset

13 of acceleration and its detection by the monitoring system, such that a timely warning is issued

14 for the implementation of consequence mitigation strategies. This paper evaluates the

15 performance of three filtering methods (simple moving average, Gaussian-weighted moving

16 average, and Savitzky-Golay), and considers their comparative advantages and disadvantages.

17 The evaluation utilized six levels of randomly generated scatter on synthetic data as well as high-

18 frequency global navigation satellite system (GNSS) displacement measurements at the Ten-mile

19 landslide in British Columbia, Canada. The simple moving average method exhibited significant

20 disadvantages compared to the Gaussian-weighted moving average and Savitzky-Golay

21 approaches. This paper presents a framework to evaluate the adequacy of different algorithms

22 for minimizing monitoring data scatter.

23 **Keywords:** Landslide; Early Warning System; Scatter; Filter; Gaussian-Weighted Moving

24 Average, Savitzky-Golay

1. Introduction

Landslides are associated with significant losses in terms of mortality and financial consequences in countries all over the world. In Canada, landslides have cost Canadians approximately $10 billion since 1841 (Guthrie, 2013) and more than $200 million annually (Clague and Bobrowsky, 2010). Essential infrastructure, such as railways and roads that play vital roles in the Canadian economy, can be exposed to damage if it transverses landslide-prone areas. Attempting to completely prevent landslides is typically infeasible, as stabilizing options and realignment may be cost-prohibitive or lead to environmental damage. This accentuates the significance of adopting strategies that require constant monitoring to mitigate the consequences of sudden landslide collapses (Vaziri et al., 2010; Macciotta and Hendry, 2021).

In recent years, detailed studies have addressed the use of early warning systems (EWSs) as a robust approach to landslide risk management (Intrieri et al., 2012; Thiebes et al., 2014; Atzeni et al., 2015; Hongtao, 2020). The United Nations defines an EWS as "a chain of capacities to provide adequate warning of imminent failure, such that the community and authorities can act accordingly to minimize the consequences associated with failure" (UNISDR, 2009). Although an EWS comprises various components acting interactively, the core of its performance relies on its ability to detect the magnitude and rate of landslide displacement (Intrieri et al., 2012). Given that the timely response of an EWS determines its effectiveness, an accurate sense of landslide velocity and acceleration is necessary. Monitoring instruments able to provide real-time or near real-time readings such as global navigation satellite systems (GNSSs) and some remote sensing techniques are, satisfactory for this purpose (Yin et al., 2010; Tofani et al., 2013; Benoit et al., 2015; Macciotta et al., 2016; Casagli et al., 2017; Chae et al., 2017; Rodriguez et al., 2017, 2018, 2020; Huntley et al., 2017; Intrieri et al., 2018; Journault et al., 2018; Carlà et al., 2019; Deane, 2020; Woods et al., 2020, 2021). These instruments can record the displacement of locations at the surface of the landslide with a high temporal resolution, which allows the monitoring system to track movements on the order of a few millimeters per year. In practice, the results are usually

52 obscured by the presence of scatter, also known as noise, and outliers that affect the quality of

53 observations. These unfavorable interferences do not reflect the true behavior of the ground

54 motion and stem from sources such as the external environment and the quality of the

55 communication signals and wave propagation in the case of remote sensing techniques (Wang,

56 2011; Carlà et al., 2017b).

57 Scatter can be defined as measurement data that are distributed around the "true" displacement

58 trend, such that the average difference between the scatter and the displacement trend is zero

59 and has a finite standard deviation. Scatter in displacement measurements can significantly

60 impact the evaluation of slope movements performed on unfiltered data and decrease the

61 reliability of an EWS. This can lead to false warnings of slope acceleration or unacceptable time

62 lags between the onset of slope failure and its identification, and therefore a loss of credibility for

63 an EWS (Lacasse and Nadim, 2009). As a result, scatter should be reduced as much as possible

64 without removing the true slope displacement trends. The application of algorithms that work as

65 filters aims to minimize the amplitude of measured scatter around the displacement trend.

66 Several approaches have been proposed to filter displacement measurements based on either

67 the frequency or time domain. Fourier and wavelet transformations aim to find the frequency

68 characteristics of the data, then attenuate or amplify certain frequencies. These approaches are

69 discussed in Karl (1989), who suggests they are generally unsuitable for non-stationary data such

70 as monitoring data time series. Filters that work on the time domain can be classified as recursive,

71 kernel, or regression filters. Recursive filters, such as the exponential filtering function, calculate

72 the filtered value at a given time based on the previous filtered value. Kernel filters, which include

73 simple moving average (SMA) and Gaussian-weighted moving average (GWMA), calculate the

74 filtered values as the weighted average of neighboring measurements. Of these two kernel filters,

75 SMA is frequently used in the literature largely due to its simplicity (Dick et al., 2015; Macciotta et

76 al., 2016, 2017b; Carlà et al., 2017a,b, 2018, 2019; Bozzano et al., 2018; Intrieri et al., 2018;

77 Kothari and Momayez, 2018; Chen and Jiang, 2020; Zhou et al., 2020; Deng et al., 2021; Desrues

78   et al., 2021; Grebby et al., 2021; Zhang et al., 2021a,b). Regression filters calculate the filtered

79   values by means of regression analysis on unfiltered values (e.g., Savitzky-Golay, or S-G)

80   (Savitzky and Golay, 1964; William, 1979; Cleveland, 1981; Cleveland and Devlin, 1988; Reid et

81   al., 2021). Carlà et al., (2017b) studied both SMA and exponential filtering on multiple failed

82   landslide cases and concluded the latter is inferior in terms of accuracy of failure time prediction.

83   On the other hand, Carri et al. (2021) cautioned the designers and users of EWSs against the use

84   of SMA when rapid movements are expected. However, published applications of filters other

85   than SMA for landslide monitoring are scarce, and studies dedicated to comparing the

86   functionality of other filters to that of SMA are limited.

87   This paper presents an approach to detect and remove outliers, evaluates the performance of

88   three filters (SMA, GWMA, and S-G), and assesses their suitability to be utilized in an EWS. We

89   evaluated three filters against the following criteria: 1) scatter is minimized, 2) true underlying

90   displacement trends are kept with as little modification as possible, and 3) filtered displacement

91   trends detect acceleration episodes in a timely manner. Moreover, the paper investigates the

92   significance of the time lag between a landslide acceleration event and its identification by a

93   monitoring system for the three filters evaluated.

94   **2. Methodology**

95   **2.1. Synthetic Data Generation**

96   A numerical analysis on a synthetic dataset approach was adopted, which consists of synthetic

97   dataset scenarios generated to resemble typical landslide displacement measurements, including

98   acceleration and deceleration periods. These scenarios are idealizations based on observations

99   of typical landslide displacements published in the literature (Leroueil, 2001; Intrieri et al., 2012;

100   Macciotta et al., 2016; Schafer, 2016; Carlà et al., 2017a; Scoppettuolo et al., 2020). A total of 12

101   dimensionless scenarios were built, with all data between the coordinates $x=0$, $y=0$ and $x=1$, $y=1$.

102   The x value represents time, and normalization between 0 and 1 allows for extrapolation of the

103 findings for variable displacement measurement frequencies (e.g., the full range of x could

104 represent a week, a month, a year). The analysis of synthetic data focuses on the ability of

105 different algorithms to minimize scatter and identify changes in measured trends; therefore, y

106 represents any of the displacement measurement metrics of interest, e.g., displacement,

107 cumulative displacement, velocity, inverse velocity, etc. Mathematical equations and graphical

108 illustrations of the 12 scenarios are shown in Fig. 1.

109 Nine of the scenarios are referred to as harmonic scenarios, which are characterized by gradual

110 changes in the trend of parameter y. The remaining three scenarios show sudden variations at or

111 near x=0.5, and are referred to as instantaneous scenarios. Considering the discrete nature of

112 instrument measurements, and to account for different ranges in measurement frequencies, each

113 scenario was generated several times, each time with a different number of points (Table 1).

114
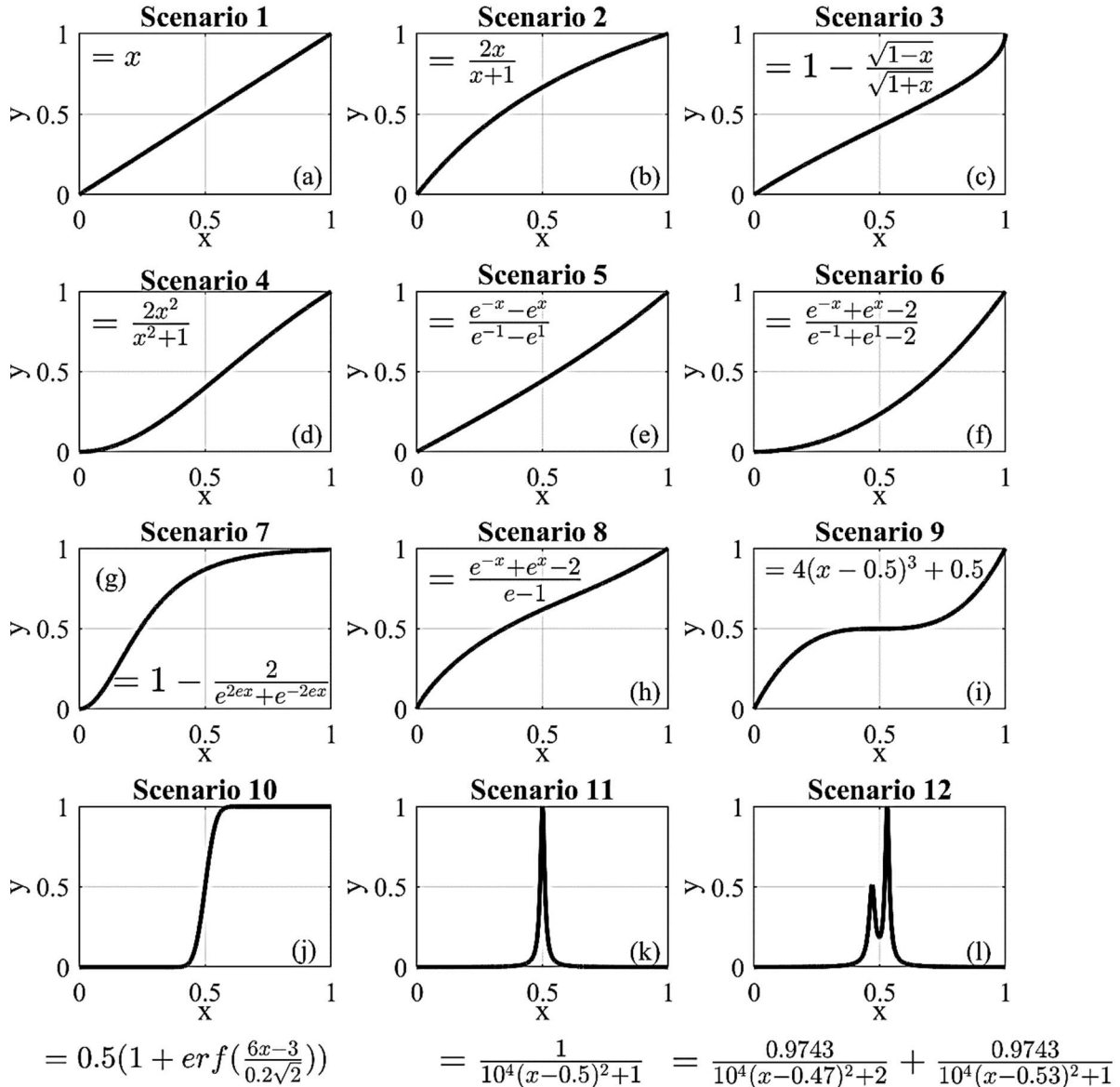
Fig. 1 Configuration of all synthetically generated scenarios

Table 1 Number of points used to generate scenarios and examples of their corresponding time spans represented by the range of x from 0 to 1 if the measurement frequency is known (1-h and 1-m readings for illustrative purposes).

Number of points	Example monitoring frequency			
	1-h readings		1-m readings	
1000	41.7	Days	16.7	Hours
3000	4.1	Months	2.1	Days
9000	1.0	Years	6.3	Days

20000	2.3	Years	2.0	Weeks
40000	4.6	Years	4.0	Weeks
86000	9.8	Years	2.0	Months
250000			5.8	Months
500000			0.9	Year
750000			1.4	Years
1.00E+6			1.9	Years

120

121   The next step was adding random scatter to the scenarios to represent unfiltered displacement

122   measurements. Macciotta et al. (2016) show the scatter in displacement monitoring for a GNSS

123   used in their analyses fitted a Gaussian distribution. We validated the scatter distribution fit

124   approximates a Gaussian distribution for the displacement data scatter of the case study in this

125   paper. This assumption, however, has an underpinning theoretical base established by the central

126   limit theorem in probability theory. It states that the mathematical summation of independent

127   variables (such as scatter) goes toward a Gaussian distribution (Smith, 2013). As a result, the

128   scatter was randomly produced from a normal distribution centered at zero, with extreme values

129   truncated between −1 and 1 and a standard deviation of 0.20. Random generation of the scatter

130   followed the techniques outlined in Clifford (1994) known as the acceptance-rejection method,

131   which generates scatter values through a series of iterations until the algorithm generates the

132   initial normal distribution. The amplitude of the scatter around the trend in parameter y was defined

133   for each scenario by scaling the randomly generated scatter. This allowed for the investigation of

134   the effect of different scatter magnitudes on the performance of the filters. Scaling was done by

135   defining the ratio n/t, which is the ratio of scatter amplitude (maximum deviation around the trend,

136   termed n) to the range of values of the trend (t) in each scenario. Six levels of n/t (0.001, 0.005,

137   0.010, 0.050, 0.100, and 0.150) were considered when performing the analysis to cover a range

138   of possible levels of scatter in unfiltered measurements. Fig. 2 shows two samples of synthetic

139 unfiltered scenarios that are the result of superimposing scatter with *n/t* values of 0.05 and 0.10,

140 respectively, on scenario No. 7.
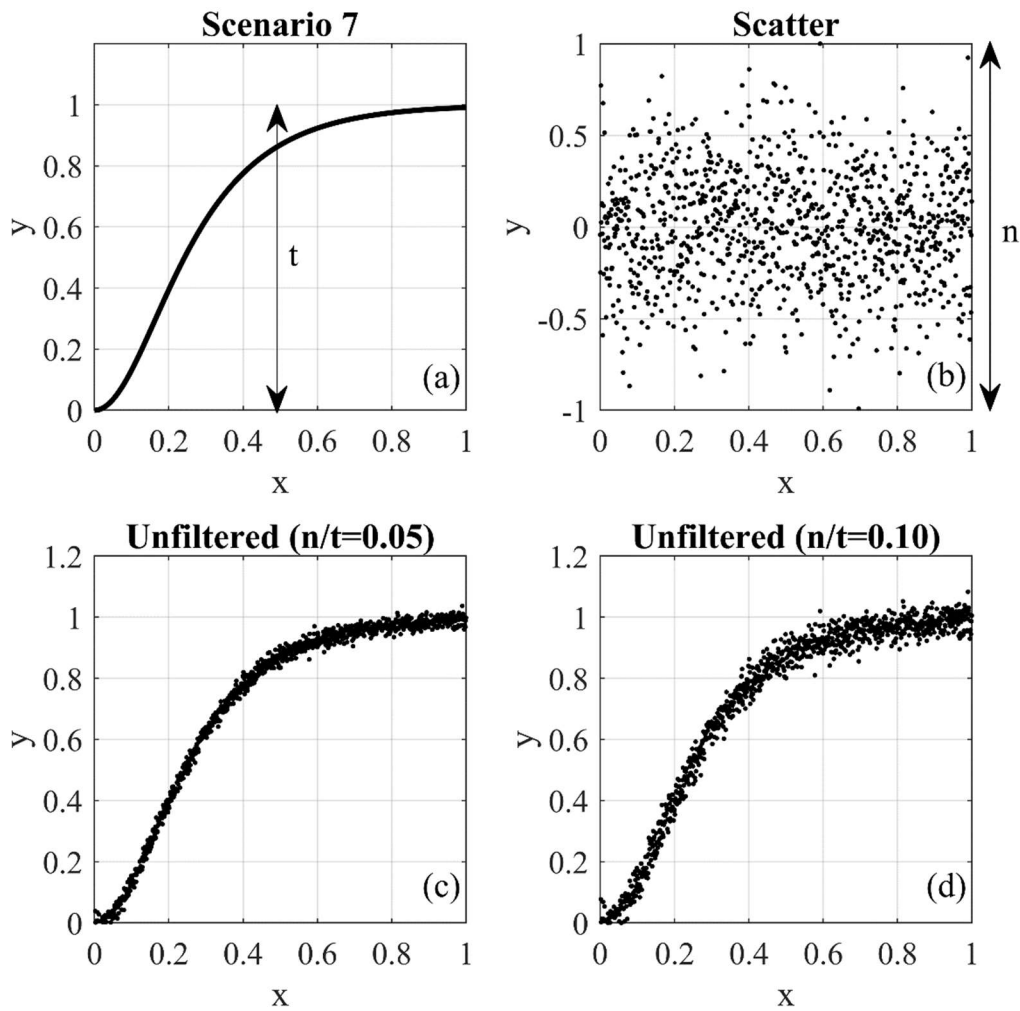
141

142 *Fig. 2 The procedure of generating a scenario with scatter: (a) generated scenario trend, (b) randomly*
143 *generated scatter, and two scenarios with scatter based on n/t values of (c) 0.05 and (d) 0.10*

144 **2.2 Data Processing Approaches**

145 *2.2.1. Simple moving average*

146 SMA is a well-known method for scatter reduction that attempts to reduce scatter by calculating

147 the arithmetic mean of neighboring points' values. A constant-length interval (window or

148 bandwidth) is used for the calculation for each point; this is also termed a "running" average.

149 Equation 1 is the formulation of this method, which was used by Macciotta et al. (2016) to analyze

150 GNSS data scatter:

$$151 \qquad \hat{y_i} = \frac{\sum_{i-\frac{p-1}{2}}^{i+\frac{p-1}{2}} y_j}{p} , \qquad (1)$$

152   where $\hat{y_i}$ is the filtered value, y_j is the unfiltered value, and p is the window length. The window

153   length is constant across the dataset except for regions near the boundaries where fewer points

154   are available. Accordingly, p will be adjusted to the number of available points that are indeed

155   less than the value set by the user. This will cause variation in the effectiveness of the method at

156   the extremes, which needs to be considered when evaluating the results of this approach.

157   *2.2.2. Gaussian-weighted moving average*

158   Varying the weights of the measurements within the calculation window in SMA can be used to

159   develop different filtering methods. The largest weight can be given to the measurement at the

160   time for which the calculation is being done, with weights decreasing for measurements farther

161   away in time. One simple weighting function that can be adopted is the Gaussian (normal)

162   distribution. Eq. 2 is the formulation of the Gaussian-weighted moving average (GWMA):

$$163 \qquad \hat{y_i} = \sum_{i-\frac{p-1}{2}}^{i+\frac{p-1}{2}} w_j y_j , \qquad (2)$$

164   where w_j is the weight coefficient based on the Gaussian distribution and the other terms follow

165   the same definition as per SMA.

166   *2.2.3. Savitkzy-Golay*

167   S-G fits a low-degree polynomial equation to the unfiltered measurements within a window and

168   defines the filtered measurements using the fitted curve (Schafer, 2011). Although this procedure

169   seems dissimilar from the weighted averaging as discussed for GWMA, its function can be

170   transformed into a kernel concept using the least-squares method if the data points are evenly

171   spaced. The detailed procedure is presented in Appendix A. Fig. 3 shows the weight kernel over

172   a window of seven points attained by fitting a quadratic polynomial. An immediate observation is

173   that some points are given negative weights. If points are not evenly spaced, the weighting kernel

174   cannot be used, and local regression analysis should be periodically conducted for each point.

175   Such filtering is known as locally estimated scatterplot smoothing (LOESS). This decreases the

176   computational efficiency of filter performance and exponentially increases the execution time.
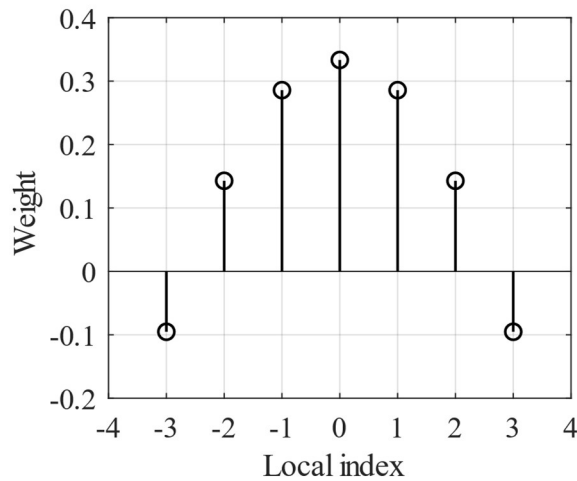
177

178   *Fig. 3 The weighting kernel of the Savitzky-Golay filter for seven points*

179   **2.3 Evaluation of Processing Algorithms**

180   The synthetic monitoring data and data from the case studies were filtered using SMA, GWMA,

181   and S-G techniques. The filters were applied with different lengths of moving windows, from 0.01

182   (1%) to 0.1 (10%) of all monitoring points, referred to as the bandwidth ratio. These limits for the

183   bandwidth ratio were selected based on literature reports for SMA. In the filtration process, we

184   only used the points prior to the time for which the calculation is being made (point of interest,

185   Fig. 4). This is to reflect the reality of displacement monitoring information as applied to EWSs.

186   To this end, filters used the first half of their kernels, but the weights were multiplied by 2 in

187   comparison to a symmetric window in order to keep the sum of weights equal to 1.
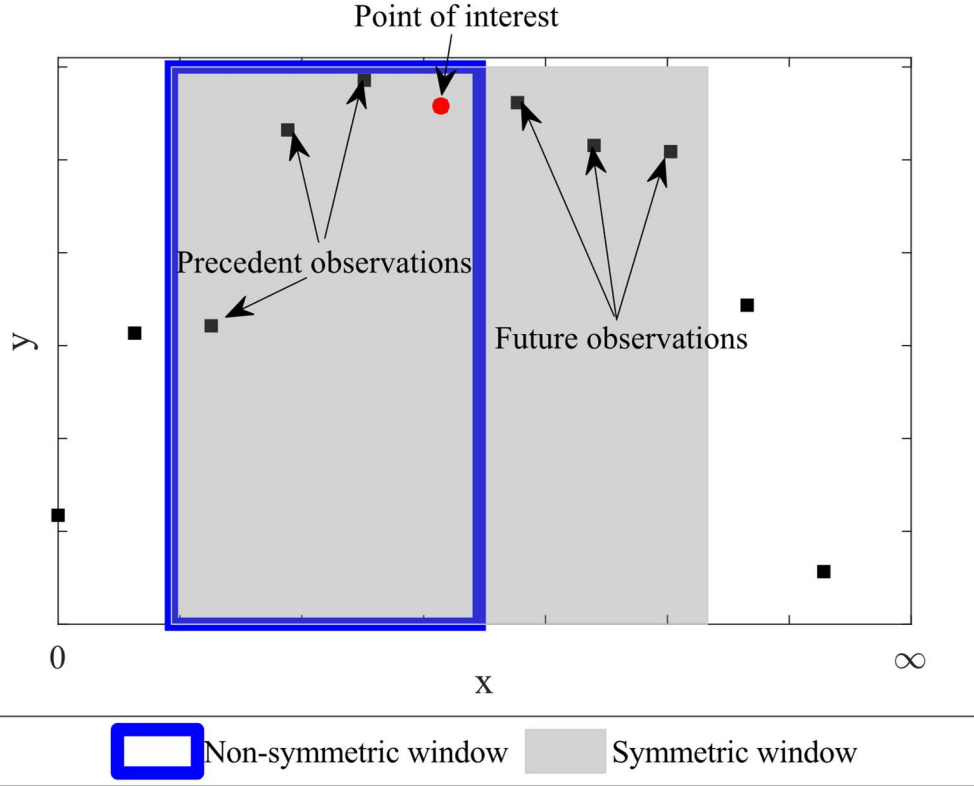
189      **Fig. 4.** *Concept of symmetric and non-symmetric window types in the filtration process*

190  All of these filters require the definition of the bandwidth. A roughness factor was defined to aid

191  in the evaluation of the effect of bandwidth in reducing scatter. This factor is defined as:

$$J_2 = \frac{\int (\hat{y}'')^2 dx}{R_a}, \tag{3}$$

$$R_a = \int (y'')^2 \, dx, \tag{4}$$

192  where J_2 is the roughness factor, $\hat{y}''$ is the second derivative of filtered measurements, R_a is the

193  absolute roughness computed by Eq. 4, and y'' is the second derivative of unfiltered

194  measurements. The second derivative measures how much the slope of the line connecting two

195  consecutive points changes, which itself is an indication of fluctuation. The greater this second

196  derivative, the greater the variation. J_2 was normalized to the overall curvature of the unfiltered

197  scenario to determine the relative scatter reduction after the application of a filter, eliminating any

198  roughness associated with the real trend in the scenario. In limit states, a value of 1 means that

199  fluctuations are similar to the unfiltered dataset, and therefore no improvement has been

200  achieved; a value of 0 suggests the slope of a scenario remains unchanged and indicates a linear

201   trend. Because all the scenarios, except the first, include trends showing concavity or convexity,

202   a residual value for the roughness factor would be expected in the lowest limit state, meaning that

203   a value of 0 is not necessarily a goal. J_2 was used to infer the minimum value of bandwidth ratio

204   after which no significant change in the fluctuation of results is achieved. Considering the second

205   power in the formulation of J_2, all observations are valid if the scenarios are mirrored (when they

206   vary from 1 to 0, instead of 0 to 1).

207   The filters are not expected to remove all scatter, and the error attributed to the residual scatter

208   can be calculated using the root mean square error (RMSE). Given that velocity values are usually

209   used as thresholds in an EWS, one concern is whether the filter should be applied to displacement

210   values or velocity values derived from unfiltered displacements. To address this issue, two

211   different approaches to filtering were investigated: direct and indirect. As a result, two different

212   approaches using the RMSE were also utilized here.

213   *2.3.1. Direct scatter filtration*

214   Direct filtration means the filter is applied to the diagram of interest. If the filtered displacement

215   values are the goal, and the filter is applied to unfiltered displacement values, then the filtering

216   process is called direct filtration. The same concept applies when velocity values are derived

217   using unfiltered displacements and the filters are then directly applied to the velocity values. In

218   this approach, the RMSE follows Eq. 5:

219
$$RMSEd = \sqrt{\tfrac{1}{m}\textstyle\sum_{i=1}^{m}(\widehat{y_\imath} - y_i)^2},\tag{5}$$

220   where *RMSEd i*s the measurement of error in direct filtration, y_i is the value of the true trend (for

221   the synthetic scenario), $\widehat{y_\imath}$ is the filtered value, and *m* is the total number of points. This approach

222   is often used in the literature (e.g., Macciotta et al., 2016; Carlà et al., 2017a,b, 2018, 2019; Intrieri

223   et al., 2018).

224   *2.3.2. Indirect scatter filtration*

225   Some EWSs can apply the filter to the displacements but use velocity trends as the metric for

226   evaluation. In this case, the filtered velocity values will be computed using the filtered

227   displacements. Indirect filtration indicates the diagram of interest is the first derivative of the

228   diagram to which the filter is applied. The RMSE, in this case, is defined as:

229 $$RMSEi = \sqrt{\frac{1}{m}\sum_{i=1}^{m}(\hat{y}_i{}' - y_i')^2}, \tag{6}$$

230   where *RMSEi i*s the measurement of error in indirect filtration, y_i' is the first derivative of the true

231   trend, $\hat{y}_i'$ is the first derivative of filtered data (derived velocity after the filter is applied to the

232   displacements), and *m* is the total number of points. Similar to J_2, all observations are valid for

233   the mirrored scenarios of those presented in Fig. 1. This is a consequence of using the second

234   power in the definition of *RMSEi* and *RMSEd*.

235   **2.4 Lag Quantification**

236   Only antecedent measurements are fed into the filters, which is expected to result in a lag between

237   the true trend and its identification by the filters. This lag means the calculated value of velocity

238   or displacement occurred sometime in the past. Consequently, reducing this lag means less time

239   is lost with respect to providing an early warning. To quantify the induced lag, the filtered diagrams

240   of all scenarios at all *n/t* ratios and bandwidth ratio values were shifted backwards a number of

241   points equivalent to 0.001 (0.1%) to 0.1 (10%) of all generated points. We refer to this as the shift

242   ratio in the rest of this paper. This shift of filtered diagrams is expected to increase their similarity

243   with the true trend until the best correlation is achieved. The R^2 test was used to determine how

244   well the shifted and filtered results replicate the underlying trend.

245   **2.5. Geocubes Differential GNSS System**

246   A Geocubes system is a network of differential global navigation satellite system (GNSS) units

247   that work with a single frequency (1572.42 MHz), making it cost-effective (Dorberstein, 2011;

248   Benoit et al., 2014; Rodriguez et al., 2018). Geocubes communicate with each other through radio

249   frequency, and a reference unit outside the boundaries of the landslide is assumed as static for

250   differential correction to increase the poor accuracy associated with single frequency GNSSs

251   (Benoit et al., 2014; Rodriguez et al., 2018). The ability of this system to achieve real-time

252   positioning, remote data collection, and processing makes it a suitable candidate for incorporation

253   into an EWS. As a result, Geocube data are used in this study to evaluate the performance of the

254   three mentioned filters.

255   **2.6. Outlier Detection**

256   Outliers are defined herein as abnormal inconsistencies (e.g., displacement directions,

257   magnitudes) when compared to the majority of observations in a random sampling of data (Zimek

258   and Filzmoser, 2018). Techniques for outlier detection have been proposed based on the

259   statistical characteristics of datasets. One common example is the Z-score method, which

260   calculates the mean and standard deviation of data within a defined interval and identifies outlier

261   data as those beyond three standard deviations from the mean (Rousseeuw and Hubert, 2011).

262   A limitation of this kind of approach is the sensitivity of the mean and standard deviation to the

263   outlier data points, which has led to the development of other methods that use other indices such

264   as the median (Salgado et al., 2016). One such technique that was adopted in this study is the

265   Hampel filter (Hampel, 1971). In this method, the median of the displacement measurements

266   within a running bandwidth is calculated and data outside a defined threshold from the median

267   are identified as outliers. The threshold is defined as a constant (threshold factor) multiplied by

268   the median absolute deviation. An asymmetric window with a bandwidth ratio of 0.004 (0.4%) and

269   a threshold factor of three were adopted following previous studies (Davies and Gather, 1993;

270   Pearson, 2002; Liu et al., 2004; Yao et al., 2019). The data identified as outliers were then

271   removed from the dataset.

272   **3. Study Site – Ten-mile Landslide**

273   The Ten-mile landslide is located in southwestern British Columbia (BC), in the Fraser River

274   Valley north of Lillooet (Fig. 5a). It is a reactivated portion of a post-glacial earthflow (Bovis, 1985)

275   that was first recognized in the 1970s. The landslide velocity has increased from an average of 1

276   mm/day in 2006 to 6 mm/day in 2016, with a maximum measured velocity of 10 mm/day (Gaib et

277   al., 2012; BGC Engineering Inc., 2016). The movement of this landslide impacts the integrity of

278   BC Highway 99 and a section of railway operated by Canadian National Railway (CN) (Carlà et

279   al., 2018), with most movement limited to the volume downslope from the railway due to the

280   installation of a retaining wall (Macciotta et al., 2017a). Despite the stabilization work done to date,

281   the uppermost tension crack has retrogressed approximately 200 m in 45 years and is now

282   situated 60 m upslope of the railway track (Macciotta et al., 2017b). The landslide lateral extents

283   have not expanded since 1981 according to the aerial photographs Macciotta et al., 2017b). The

284   Ten-mile landslide is currently approximately 200 m wide, 140 m high, and has a volume of 0.75

285   to 1 million m^3, moving towards the Fraser River on a continuous rupture surface with a dip of

286   about 22 to 24°, which is sub-parallel to the ground surface (Rodriguez et al., 2017; Donati et al.,

287   2020). The elevation of the shear surface and mechanism of the landslide have been inferred

288   from the readings of multiple slope inclinometers installed in 2015 (BGC Engineering Inc., 2015).

289   The bedrock in this region consists of volcanic rocks, such as andesite, dacite, and basalt, and is

290   overlain by Quaternary deposits (Donati et al., 2020; Carlà et al., 2018; Macciotta et al., 2017a).

291   The thickness of the landslide varies between 20 and 40 m and the ground profile from the surface

292   to depth comprises medium to high plastic clays and silts overlying colluvium material and glacial

293   deposits, overlying bedrock (BGC Engineering Inc., 2015). The stratigraphy of the sedimented

294   soils in the landslide area notably varies from one borehole to another and reflects the complex

295   stratigraphy of the earthflow.

296   A total of 11 Geocubes were installed at the Ten-mile landslide in 2016. Fig. 5b is a front view of

297   the landslide showing the locations of the Geocube units. Units 44 and 50 are installed near the

298   uppermost tension crack identified as the current landslide backscarp, unit 69 is 30 m above the

299   backscarp, and unit 39 is used as the reference point. Please note that unit 69 is used as the fixed

300   Geocube, and is not shown in Fig. 5b. The other units are located within the boundaries of the

301   landslide, with a maximum distance between units of 310 m (Rodriguez et al., 2018). The time

302   step between every two consecutive measurements is 60 s. Fig. 6 shows the displacements of

303   units 46 and 47, which were the largest in comparison to other Geocubes.
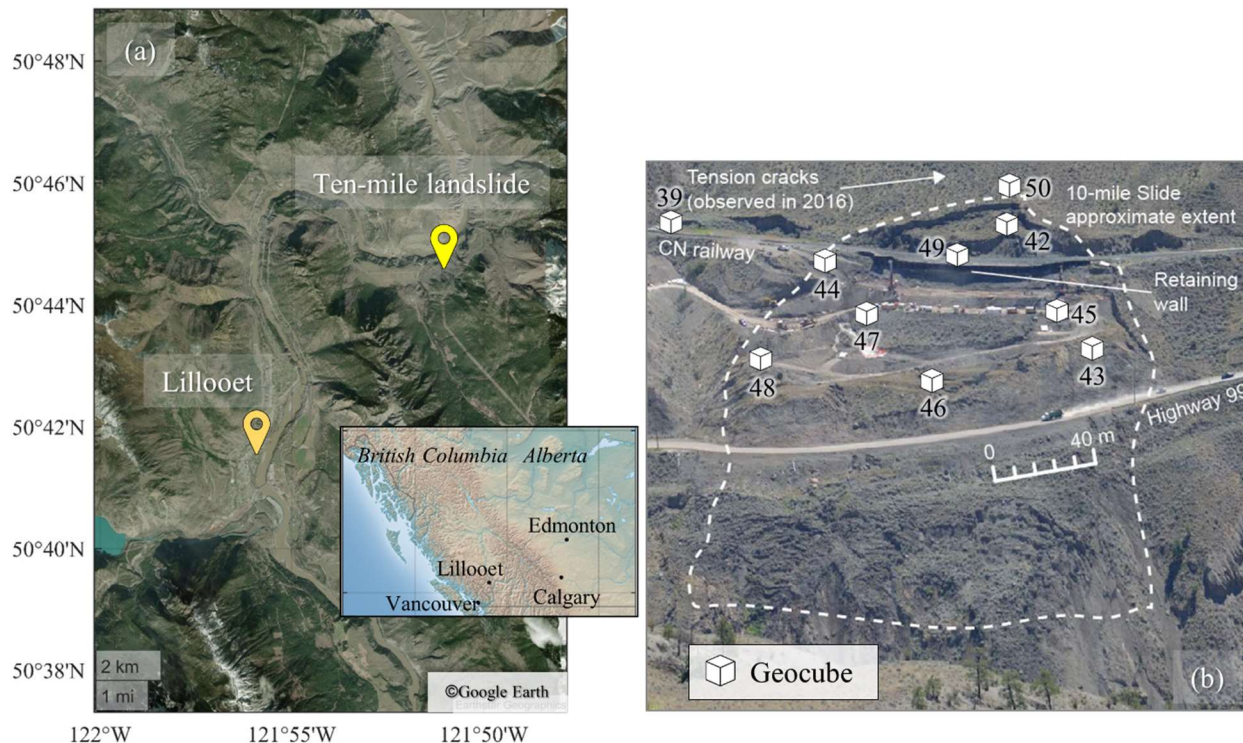
304
305   **Fig. 5** (a) Location of the Ten-mile landslide (© Google Earth) and (b) front view of the Ten-mile landslide
306   and distribution of Geocubes on its surface (Rodriguez et al., 2018; Macciotta et al., 2017b)
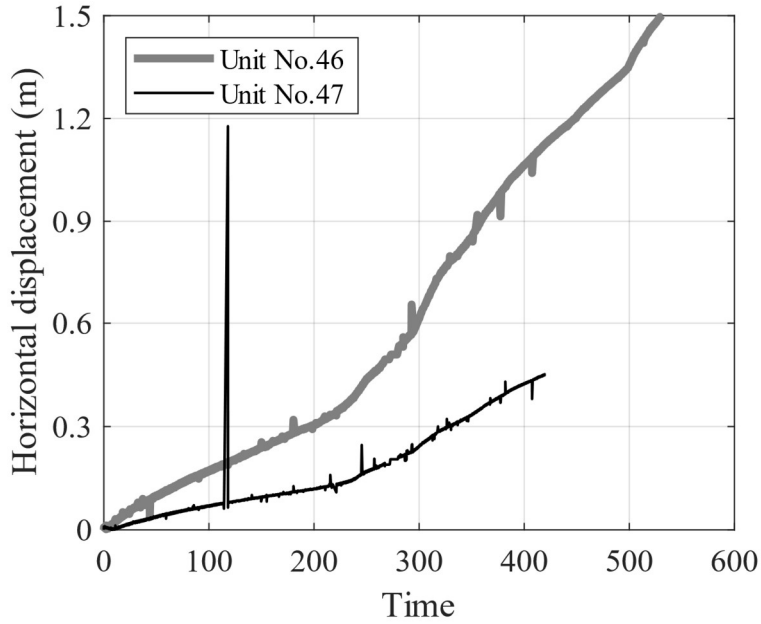
307
308 ***Fig. 6*** *Cumulative horizontal displacement of Geocube units No. 46 and 47*

309 **4. Results**

310 **4.1. Synthetic Analysis**

311 Fig. 7 shows the roughness value (J_2) of scenario 6 for SMA, GWMA, and S-G on a semi-

312 logarithmic scale. This figure illustrates how, regardless of the n/t ratio, J_2 substantially decreases

313 as the bandwidth ratio increases to 0.01 and then asymptotically approaches a final value. This

314 means that increasing the bandwidth ratio drastically reduces scatter; however, its effectiveness

315 is restricted as the bandwidth ratio increases above 0.01. This observation was consistent for

316 other scenarios. J_2 values (including scenario 6 in Fig. 7) indicate that J_2 approaches its minimum

317 at bandwidth ratio values of 0.03 to 0.04, regardless of the filter selected.
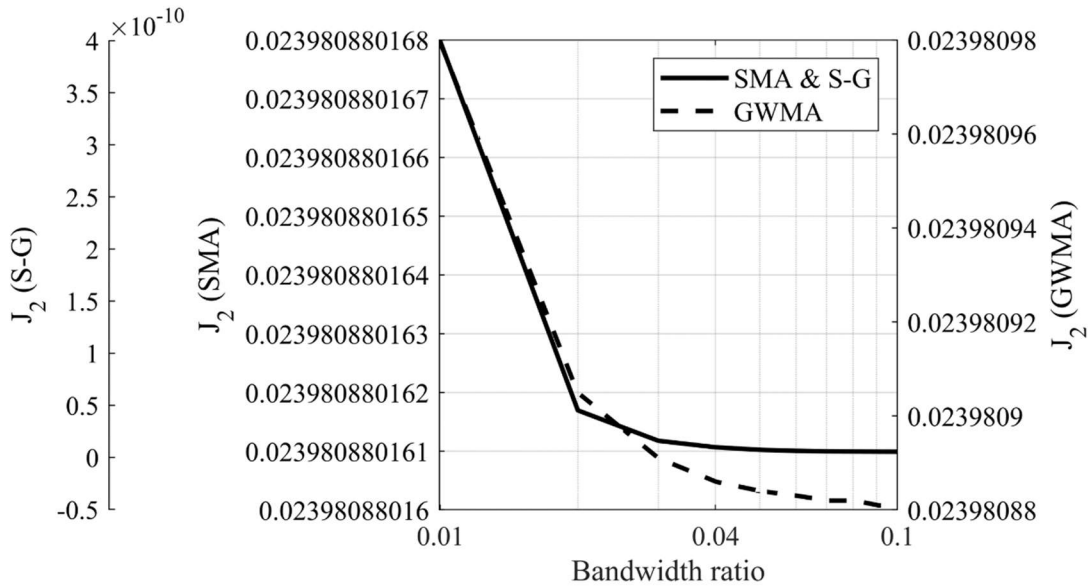
318

319   ***Fig. 7*** *Variation of roughness factor for scenario 6 with respect to the applied filter on a semi-log scale*

320   *4.1.1. Effect of filters on trend distortion*

321   Scenarios 11 and 12 were first analyzed to evaluate the degree to which the trend was preserved

322   by these filters, as peaks made it easier for visualization. Fig. 8a shows the true trend of scenario

323   11 along with two SMA-filtered scenarios at bandwidth ratios of 0.04 and 0.10, respectively. This

324   figure shows that, as the SMA filter bandwidth increases, the peak in measurements is identified

325   at a later time than the true trend (x=0.5) and the magnitude of the peak is reduced (more than

326   70% reduction at a bandwidth ratio of 0.10). Furthermore, as the bandwidth ratio increases, the

327   "instantaneous" nature of the peak is lost to a more transitional variation. This highlights a

328   disadvantage of SMA when handling sudden changes in data trends. The calculated *x* value of

329   the peak in scenario 11 is plotted for different bandwidth ratios and for all three filters in Fig. 8b.

330   This figure shows the time at which the peak is identified lags as the bandwidth ratio increases

331   for all filters; however, GWMA and S-G identify the peak with a much smaller lag, independent of

332   the *n*/*t* ratio. As an example, for a year of monitoring data at a frequency of 30 s and bandwidth

333   ratio of 0.10, SMA, GWMA, and S-G predict the peak point approximately 17, 3.5, and 2.7 days

334   after the real peak, respectively. This lag can be attributed to the utilization of an asymmetric

335   window, which leads to a lagged response of the filter. As more points are included in the filtering

336   procedure (increasing bandwidth ratio), this lag increases because the averaging process is

337   sensitive to window type. The degree of sensitivity, however, depends on the filter. Fig. 8c shows

338   the variation of the peak magnitude with respect to the bandwidth ratio for all three filters. SMA

339   and GWMA both underestimate the peak value, and the difference between the calculated peak

340   and real peak increases as the bandwidth ratio increases. SMA calculations underestimate the

341   peak more than twice as much as GWMA. On the contrary, S-G intensifies the peak up to a

342   bandwidth ratio of 0.04, with the impact tending to diminish at larger bandwidth ratios; it predicts

343   the true value at a bandwidth ratio value of almost 0.09.
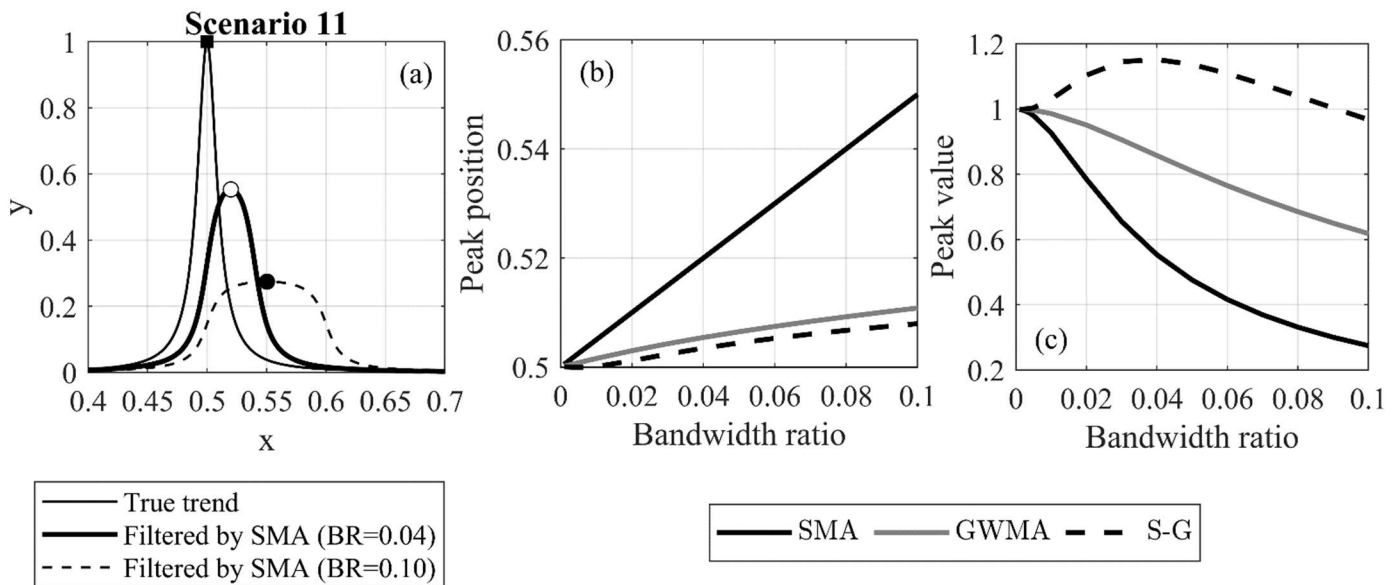
344
345   **Fig. 8** *(a) An example of peak displacement by applying SMA, and variation of (b) peak position and (c)*
346   *peak value with respect to the filter and bandwidth ratio used (original peak at 0.5)*

347   Scenario 12 was used for a detailed evaluation of the ability of these filters to conserve the

348   underlying original trend.**Error! Reference source not found.** Fig. 9 shows scenario 12 and the

349   filtered results for all three filters and an *n*/*t* ratio of 0.15. This scenario and these specific

350   parameters were selected for illustration purposes as they allow visual identification of differences

351   for discussion. The SMA filter considerably underestimates the magnitude of the peak at a

352   bandwidth ratio of 0.04, which should be the minimum bandwidth ratio according to Fig. 7. At a

353   bandwidth ratio of 0.10, the filtered diagram is distorted in comparison to the true trend and the

354   initial peak is not identified. GWMA at a bandwidth ratio of 0.04 shows less underestimation of

355   the peak magnitude, and a slight lag is visually observed at a bandwidth ratio of 0.10. This

356   indicates the significantly better performance of GWMA over SMA. S-G results for both bandwidth

357   ratios closely identify the time and magnitude of both peaks, indicating yet better performance.

358   However, the peak is artificially intensified at a bandwidth ratio of 0.04, and a significant drop

359   occurs well beyond the true trend immediately after the second peak for both bandwidth ratios

360   (pulsating effect), which was also observed in scenario 11. Increasing the degree of the

361   polynomial fitted as part of the S-G methodology was not completely effective at eliminating this

362   effect. The pulsating effect was also observed when a symmetrical window was utilized and is

363   attributed to the negative weights in the S-G kernel.
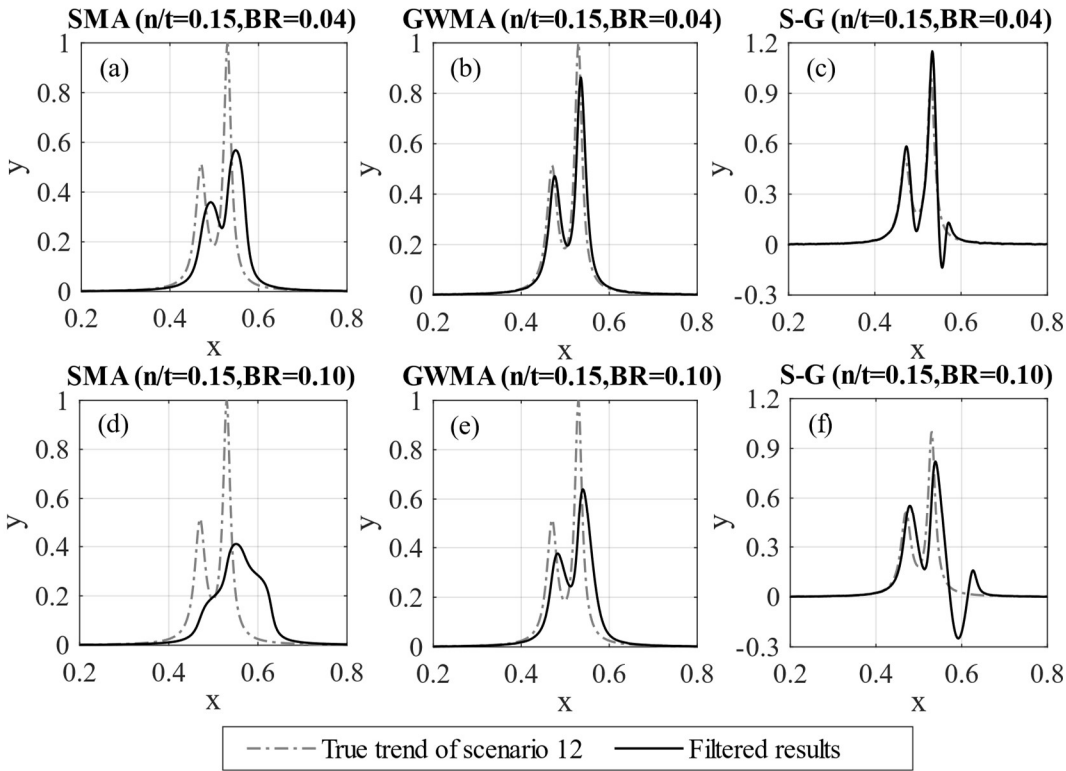
364

365
366   **Fig. 9** *Filtered results of Scenario 12 with scatter using SMA (a,d), GWMA (b,e), and S-G (c,f) at*
367   *bandwidth ratios (BRs) of 0.04 (a-c) and 0.10 (d-f)*

368   *4.1.2. Results of direct scatter filtration*

369   Fig. 10 shows the RMSEd of all three filters for all the harmonic synthetic scenarios. This figure

370   shows that, for these numerical analyses on synthetic scenarios, the error depends linearly on

371   the bandwidth ratio for all of the filters and does not depend on the scenario or n/t ratio. SMA

372   shows the greatest difference from the true trend, followed by GWMA (approximately 60% less

373   difference than SMA). S-G, on the other hand, almost lies on the horizontal axis for all the

374   bandwidth ratios, which means the filtered results yield near-zero error. Fig. 10 also shows how

375   the error increases as the bandwidth ratio increases. This can be attributed to the utilization of an

376   asymmetric window, which leads to a lagged response of the filter. As more points are included

377   in the filtering procedure (increasing bandwidth ratio), this lag increases and, consequently,

378   causes a larger error. The RMSEd of filters for the instantaneous synthetic scenarios are shown

379   in Fig. 11. In scenario 10, the same behavior as noted for the harmonic scenarios can be seen

380   for SMA and GWMA, whereas S-G is not as accurate. This is more noticeable in scenarios 11

381   and 12 in which S-G becomes less accurate than GWMA at larger bandwidth ratios. This result

382   shows that S-G cannot handle the instantaneous scenarios as satisfactorily as the harmonic ones.

383   The errors related to SMA and GWMA for the instantaneous synthetic scenarios show non-linear

384   behavior and are greater when compared to the harmonic scenarios. Fig. 11 clearly shows all

385   filters are challenged by the instantaneous variations when compared to gradual ones in direct

386   filtration.
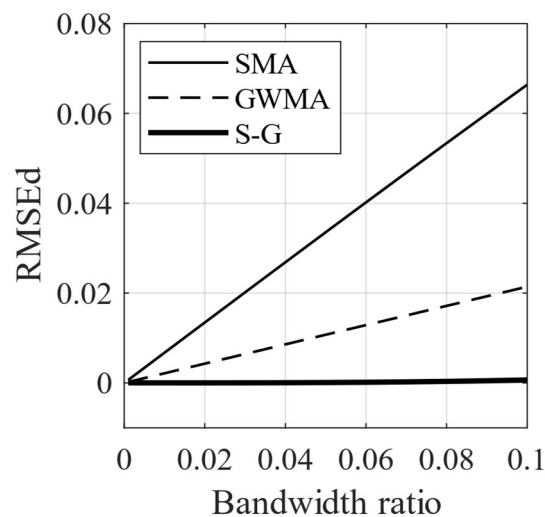
387
388   ***Fig. 10*** *RMSEd for the harmonic scenarios*
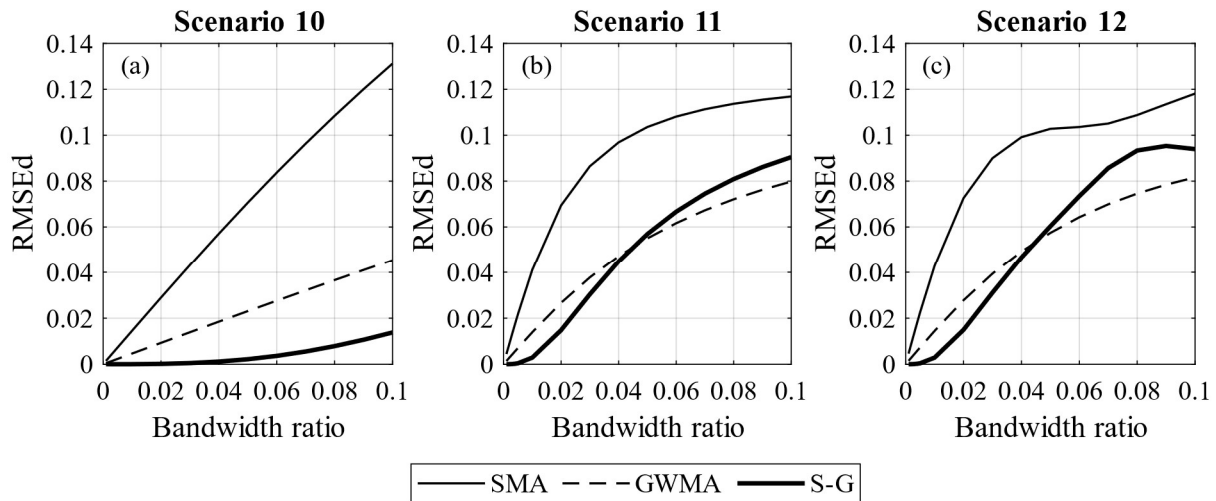
Fig. 11 *RMSEd for the instantaneous scenarios*

4.1.3. Results of indirect scatter filtration

Fig. 12 shows the RMSEi results for the harmonic scenarios (when performing indirect filtration) on a semi-logarithmic scale. We observed that the error considerably decreases as the bandwidth ratio increases to 0.02; however, to highlight the variation of error in the range of interest for the bandwidth ratio, only RMSEi values corresponding to bandwidth ratios greater than 0.04 are plotted in Fig. 12 and 13. In Fig. 12, the error for the GWMA is either equal to or slightly less than the error for the SMA, and S-G shows the least error for the harmonic scenarios. The RMSEi results for the instantaneous scenarios (Fig. 13) are similar to those for the harmonic scenarios for large n/t ratios (0.05, 0.10 and 0.15). For small n/t ratios, the GWMA is superior at bandwidth ratios above 0.06, and S-G has the worst performance.
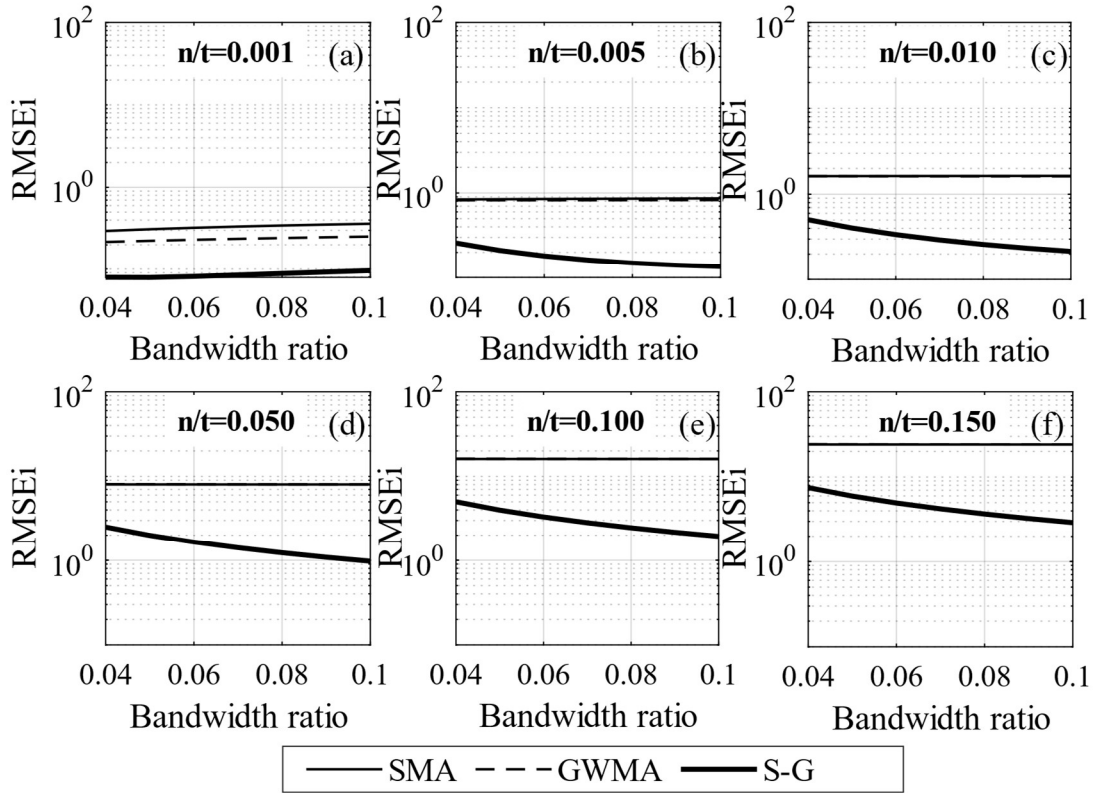
401
402   **Fig. 12** RMSEi for the harmonic scenarios on a semi-logarithmic scale
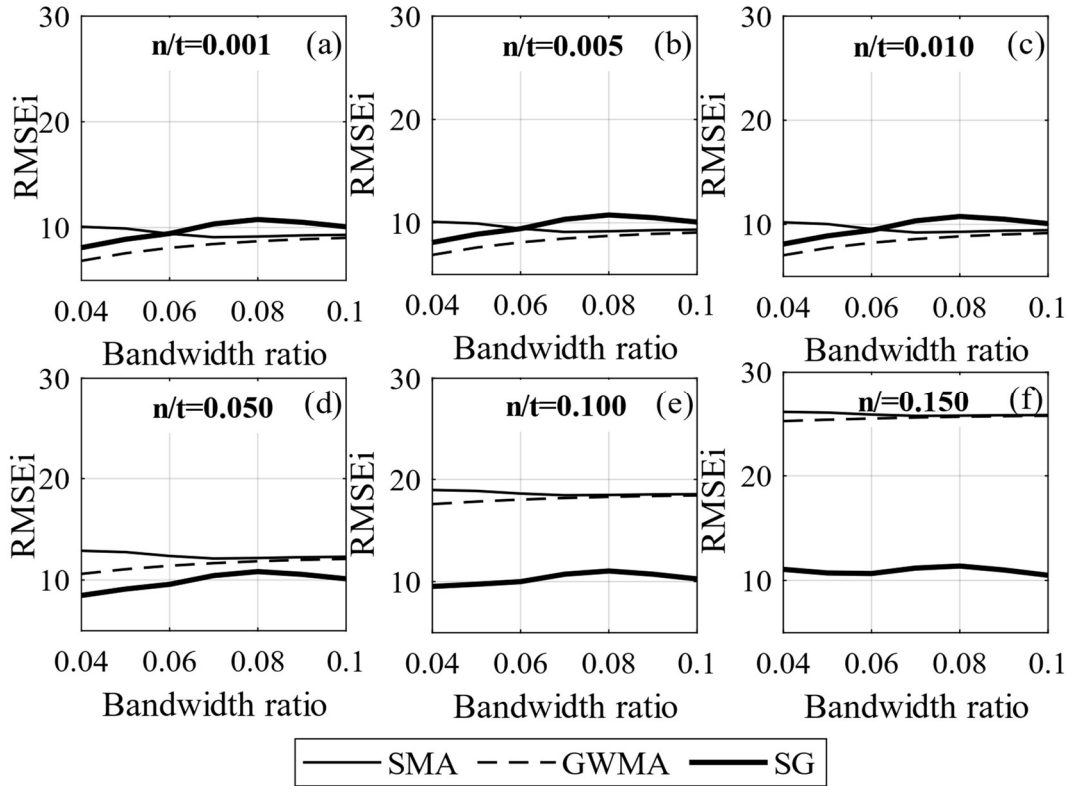
403

404   *Fig. 13 RMSEi for the instantaneous scenarios*

405   *4.1.4. Lag quantification*

406   The non-symmetric inclusion of points causes the identification of a lag in the trend of filtered

407   data. Fig. 14 shows Scenario 10 with respect to the original trend, with scatter added (at an *n/t*

408   value of 0.15), and the results after filtering with each of the three methods at a bandwidth ratio

409   of 0.04. This figure clearly shows the lag between the results filtered by SMA and GWMA and the

410   true trend. S-G results do not have as severe a lag as that resulting from the other filters; we

411   attribute this to the negative weights in its kernel that anchor the filtered values and prevent a

412   lagged response. A minor pulsating effect can be observed in the S-G filtered data, decreasing

413   the calculated values at a much earlier time than the true trend. This suggests that S-G is robust

414   with respect to identifying initial changes in monitoring trends but overcorrects subsequent

415   changes; SMA grossly lags with respect to the identification of any change, and GWMA has a

416   reduced lag when compared to SMA.
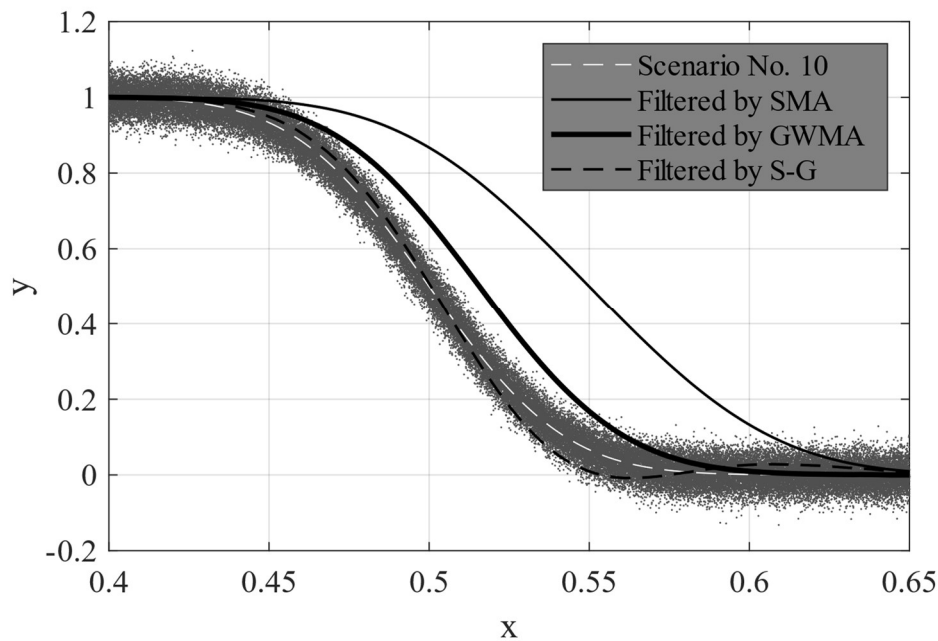
417

418   ***Fig. 14*** *Scenario 10 with and without scatter, and with scattered results filtered by SMA, GWMA, and S-G*
419   *for an n/t value of 0.15 and a bandwidth ratio of 0.04.*

420   Fig. 15a shows an example of the R^2 correlation for scenario 7, comparing the original trend and

421   the results filtered by SMA at an *n/t* value of 0.01 and bandwidth ratio of 0.04. The shift ratio is

422   the shift of filtered trends (in the horizontal axis – parameter *x*) relative to the range of *x* values.

423   R^2 calculations are shown for the filtered data (shift ratio of 0) and as the filtered trends are shifted

424   backwards in time (negative shift ratio values). In this analysis, the peak R^2 value (largest

425   correlation between the shifted filtered results and original trend) indicates the shift required to

426   minimize the lag in identifying the original trend changes, therefore providing a quantitative

427   approach to calculating the lag in parameter *x*. In the example in Fig. 15a, the lag corresponded

428   to 0.018 (1.8%) of the total points.
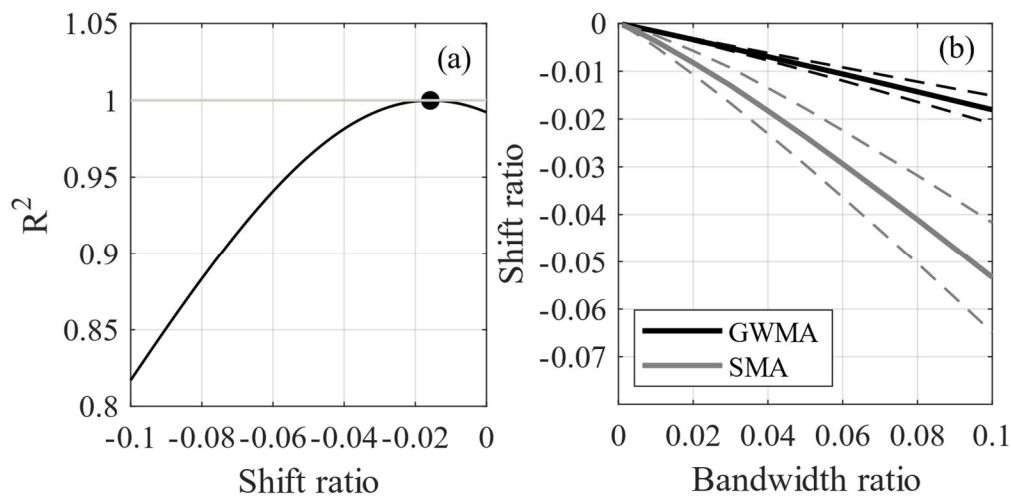
429
430   ***Fig. 15** (a) R^2 values for scenario 7 with filtered and shifted results at an n/t value of 0.01 and bandwidth*
431   *ratio of 0.04 and (b) shift ratio at peak R^2 for all scenarios and n/t ratios, with the mean (solid line)*
432   *bounded by one standard deviation (dashed lines)*

433   Peak R^2 values for all scenarios and *n/t* values are closely correlated with the bandwidth ratio.

434   The lag, quantified by the shift ratio, is larger when the trend change is more pronounced;

435   therefore, the correlation between the shift ratio and bandwidth ratio is different for different

436   scenarios. Fig. 15b shows the mean correlation between the shift ratio and bandwidth ratio, for

437   all scenarios and n/t values, bounded by one standard deviation, for GWMA and SMA. Table 2

438   shows linear and quadratic regressions of this correlation and the strength of the correlation in

439   terms of R^2 and RMSE. Fig. 15b quantitatively shows that GWMA lags less than SMA with respect

440   to identifying changes in measurement trends. Moreover, the uncertainty associated with lag for

441   SMA is greater than for GWMA because of the larger standard deviation. Fig. 15b quantifies how

442   increasing the bandwidth ratio increases the lag with respect to identifying true measurement

443   trends and, although large bandwidth ratios decrease the scatter in data, the bandwidth ratio

444   should carefully balance minimizing both scatter (J_2) and lag (shift ratio). S-G is not included in

445   this analysis as the method resulted in no significant lag in identifying changes in measurement

446   trends; however, it had the disadvantages previously noted including pulsating effects and

447   overestimating peak values.

448   **Table 2** *Regression correlations between shift ratio (SR) and bandwidth ratio (BR) with the strength of the*
449   *correlation in terms of R^2 and RMSE*

	Linear regression		Quadratic regression	
SMA	SR=-0.5087(BR)	R^2=0.9940 RMSE=0.0014	SR=-1.323(BR^2)-0.4049(BR)	R^2=0.9997 RMSE=3.24E-4
GWMA	SR=-0.1783(BR)	R^2=0.9996 RMSE=1.2963E-4	SR=-0.1171(BR^2)-0.1691(BR)	R^2=0.9999 RMSE=3.5672E-5

450   **4.2. Results on the Ten-mile landslide**

451   Unfiltered results reported by Geocubes 46 and 47 installed on the Ten-mile landslide were

452   processed by all three filters. To illustrate to the reader through visual inspection the difference

453   between the performance of SMA, GWMA, and S-G, only a 200-day window of displacement data

454   from Geocube 46 and filtered points produced by direct filtration are shown in Fig. 16. Fig. 16a

455   also features an inset showing scaled scenario 4, which resembles the general trend of Geocube

456   46 data for the period from day 200 to 400. Fig. 16 shows that increasing the bandwidth ratio

457   reduces the scatter, but increases the lag in the filtered results, consistent with observations on

458   the synthetic datasets. For bandwidth ratios larger than 0.04, SMA becomes insensitive to some

459   short-scale (20- to 30-day) trends in the data (qualitative visual inspection). As an example, at a

460   bandwidth ratio of 0.10, SMA suggests the displacement of Geocube 46 follows a bi-linear trend

461   with an inflection point at day 240, while unfiltered points and other filters suggest other periods

462   of acceleration and deceleration. Importantly, S-G is sensitive to even subtle variation and does

463   not show significant lag.
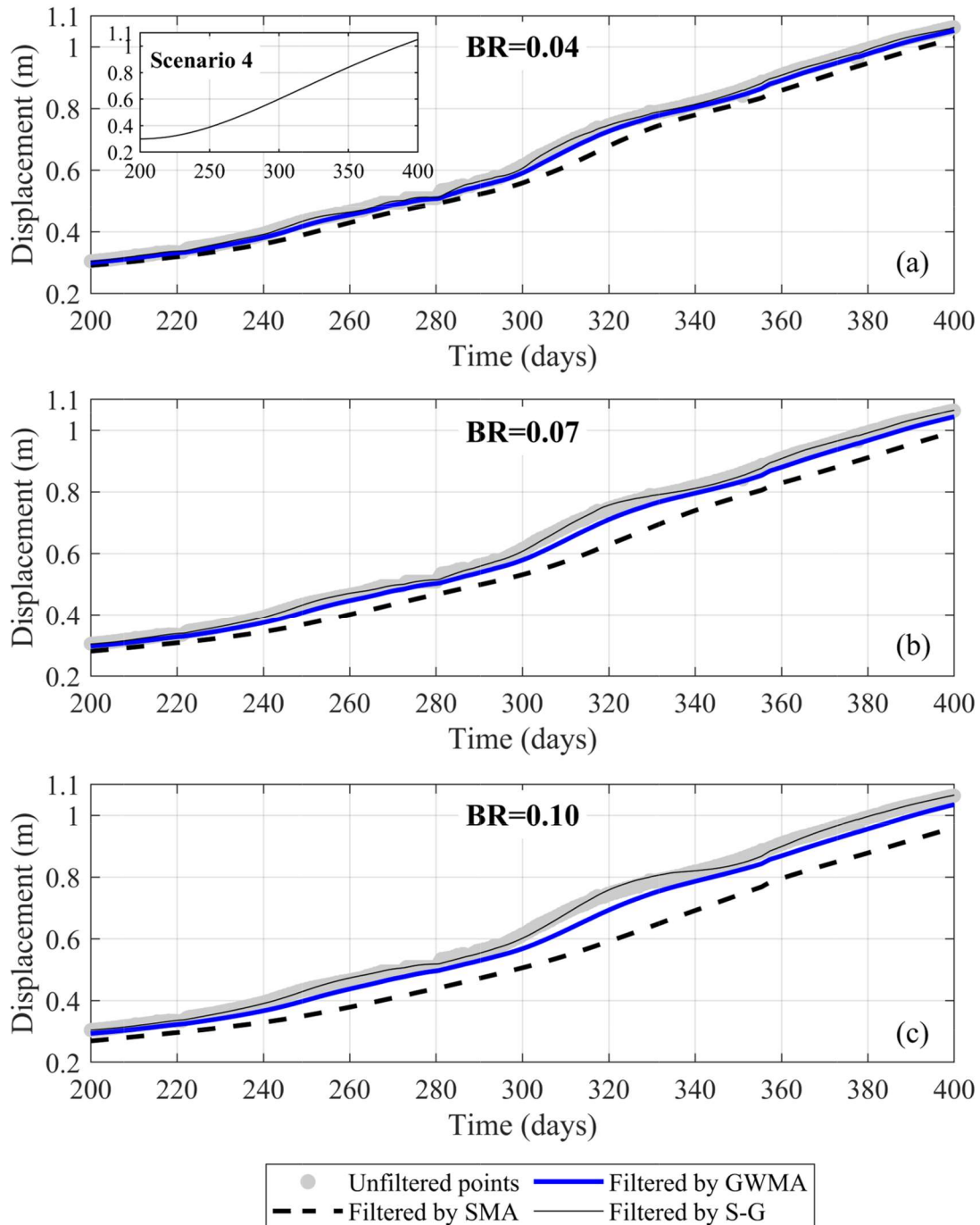
464
465   ***Fig. 16*** *Unfiltered displacement of Geocube 46 data vs. time and data filtered by SMA, GWMA, and S-G*
466   *for bandwidth ratios (BRs) of (a) 0.04, (b) 0.07, and (c) 0.10.*

467   Fig. 17 shows the filtered velocity values obtained by directly filtering the calculated velocities and

468   by indirectly filtering the displacement values before calculating the velocity from Geocube 46

469   data. The direct and indirect filtering approaches demonstrated similar performance in terms of

470   scatter reduction for Geocube 46 data. As the bandwidth ratio increases, SMA tends to

471   significantly attenuate the local maximum and minimum points in comparison to results at smaller

472   bandwidth ratios, indicating a probable loss of information about the landslide behavior and

473   sensitivity of this filter to the bandwidth ratio, as also noted in Fig. 16 (curvature loss in SMA

474   results). Indirect filtration by SMA seems to be limited near the boundary at time zero, resulting in

475   a subdued replica of direct filtration. The length of this region is found to be governed by the

476   bandwidth ratio, as the necessary number of points for filtering in this portion has not been

477   provided to the filter. This is also observed in S-G results. This problem was not found in GWMA

478   results, as direct and indirect filtration both follow the same pattern. GWMA and S-G are both able

479   to preserve the velocity variation even at the most intense filtration (bandwidth ratio of 0.10);

480   however, variations between local maxima and minima are more extreme in S-G than GWMA

481   results. This is attributed to peak overestimation (Fig. 8 and 9) or a pulsating effect superimposing

482   on the peaks/troughs. Moreover, the S-G results still demonstrate relatively large fluctuations

483   even at the largest bandwidth ratio. This means that the application of S-G might still trigger false

484   alarms in an EWS if the landslide is moving at a faster rate or experiencing different episodes of

485   acceleration and deceleration. To avoid this, a larger bandwidth ratio should be used but this can

486   be problematic due to the higher computational effort required and issues that might follow, such

487   as the pulsating effect.

488   Results for Geocube 47 confirm the same observations made for Geocube 46 but also allow for

489   an evaluation of the significance of outliers on the filtered results. Fig. 18a displays the outliers

490   detected in the displacement diagram of Geocube 47 data along with the threshold established

491   by the Hampel algorithm using an asymmetric window, a bandwidth of 0.4% and a threshold factor

492   of 3. Fig. 18b-d shows a magnified portion of the displacement measurements for Geocube 47

493   filtered by each of the three filters at three different bandwidth ratios before the elimination of

494   outliers. This highlights the necessity of outlier elimination before the application of any scatter

495   filter. These plots show that detecting and removing outliers significantly impacts the performance

496   of S-G, as the presence of the outlier generates a peak that follows the outlier measurement and

497   is followed by a sudden decrease that drops well beyond the data trend. SMA tends to widen the

498   time range affected by the outlier more than GWMA but, for the most part, the SMA-filtered results

499   are almost parallel to the underlying trend. All filters appear to be significantly impacted by the

500   outlier value, suggesting a pre-processing filter is required to remove outliers regardless of the

501   use of SMA, GWMA, or S-G to reduce scatter. The outliers were successfully identified and

502   removed after the application of the Hampel algorithm, and the above-mentioned effects were no

503   longer observed in the filtered results.
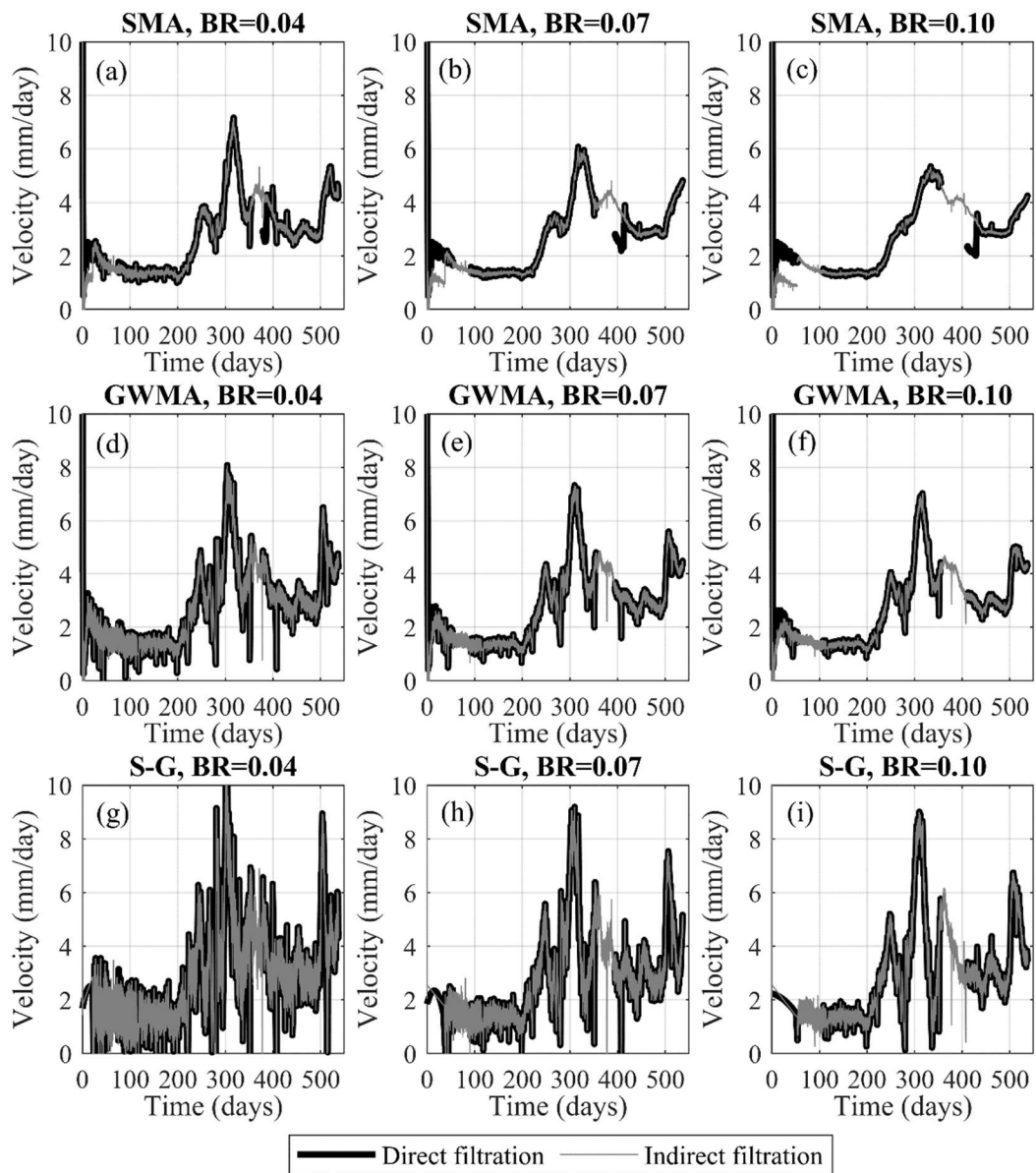
504
505 **Fig. 17** *Indirect and direct filtration results of Geocube No. 46 velocity values for bandwidth ratio (BR)*
506 *values of (a) 0.04, (b) 0.07, and (c) 0.10.*

507

508
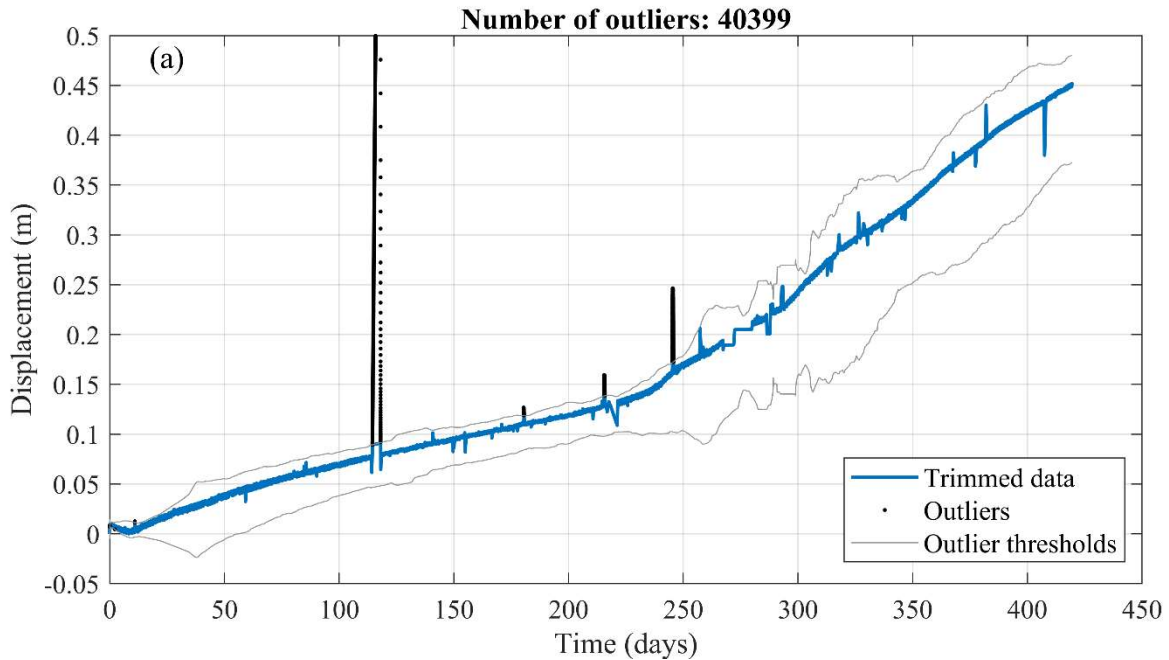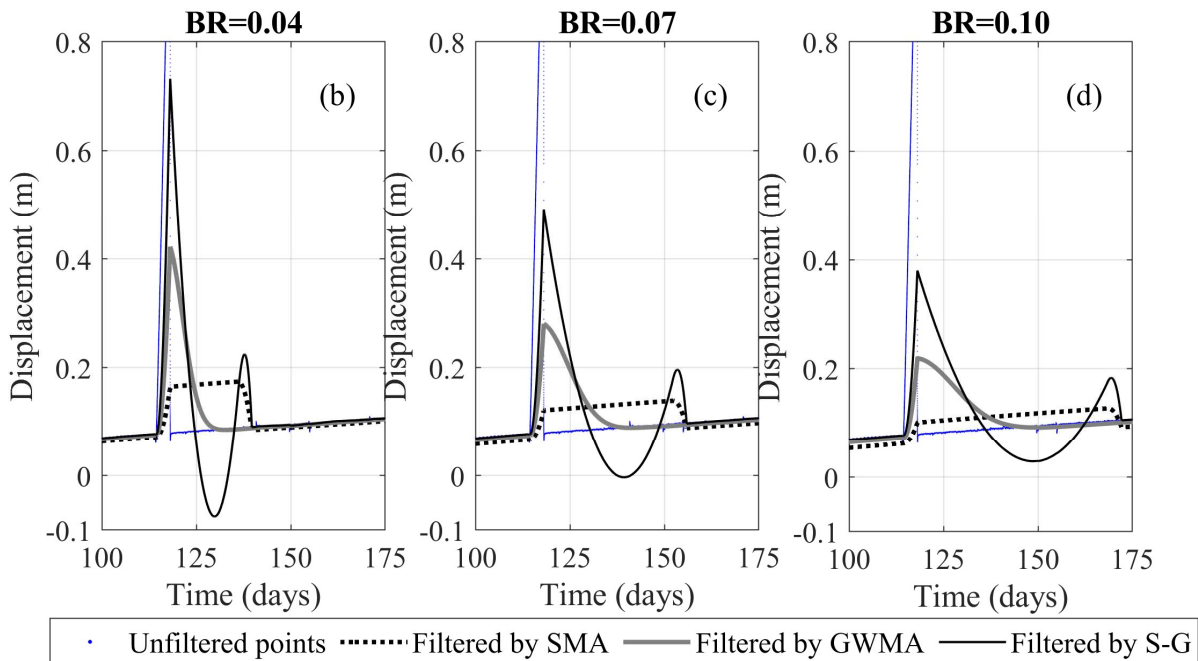
Fig. 18 Unfiltered and filtered displacement measurements for Geocube 47 at bandwidth ratios (BRs) of (a) 0.04, (b) 0.07 and (c) 0.10

4.2.1. Lag minimization in filtered Geocube results

The lag between unfiltered and filtered data for Geocube 46 (Fig. 16) is consistent with the synthetic database results. The lag quantification results (Fig. 15b) were used to provide a correction value for the filtered Geocube results. The shift ratios used for this purpose with respect

515   to each filter and bandwidth ratio are tabulated in Table 3. To determine whether the results of

516   lag correction using the mean correlations derived from the synthetic scenarios (Table 2) were

517   acceptable, the filtered diagrams were shifted (using the mean line for GWMA and values

518   between the mean and lower boundary for SMA) and different portions of the displacement

519   diagrams for Geocubes 46 and 47 were examined. Some examples are shown in Fig. 19. The

520   mean and standard deviation of the scatter around the trend (error distribution) were calculated

521   by assuming a linear trend within the short periods of analysis (considered an approximation of

522   the true displacement trend for the short time interval). These were also calculated for the filtered

523   and shifted diagrams. The closer the mean and standard deviation of the filtered and shifted data

524   are to that obtained from the linear trend, the better the performance of the lag correction based

525   on the results from the synthetic scenarios. As an example, for the period from day 250 to 260,

526   the GWMA resulted in a standard deviation of 0.001 to 0.0015 for bandwidth ratios from 0.04 to

527   0.10, respectively; corresponding values for SMA to 0.0018 to 0.0021. This illustrates that shifted

528   GWMA results are closer to the true (scatter-free) displacements because the standard deviations

529   of scatter inferred by this filter are closer to the true scatter, although both have good agreement

530   with the true scatter. The means of inferred scatter by both filters are also close enough to the

531   mean of the true scatter (almost zero). The results show the statistical indices of scatter inferred

532   from the filtered shifted displacement measurements closely agree with that considered to be true

533   scatter, and therefore the filtered displacement measurements are corrected for lag. This

534   suggests the correlations stated in Fig. 15b and Table 2 based on the synthetic scenarios are

535   applicable to minimize the lag for the Geocube system at the Ten-mile landslide.

    Table 3. Shift ratios used for lag minimization of Geocube 46 displacements

Bandwidth ratio	Shift ratio	
	SMA	GWMA
0.04	-0.02	-0.007
0.07	-0.035	-0.012
0.10	-0.06	-0.018

537
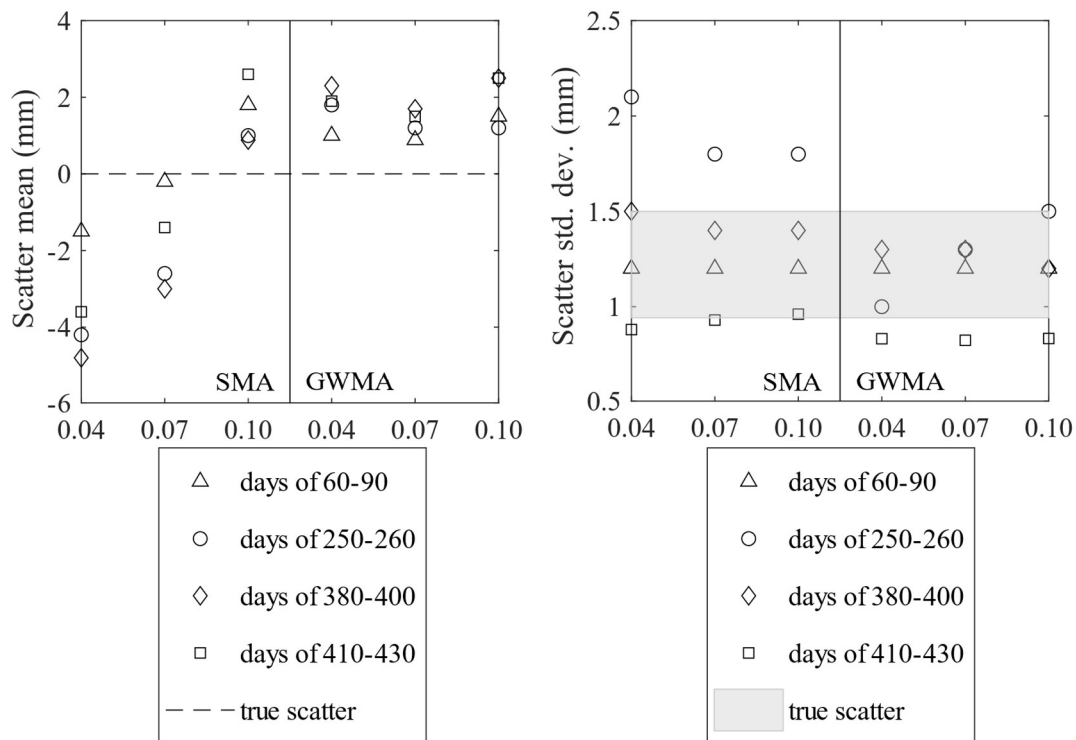
538
539   **Fig. 19.** *Mean and standard deviation of scatter inferred by SMA and GWMA in comparison with true*
540   *scatter in the displacement of Geocube 46*

541

5. Discussion

543   Previous studies dedicated to landslide monitoring consistently adopt SMA for scatter

544   minimization in displacement data. However, the adequacy of this filter and the effect of bandwidth

545   selection were not well understood. Analyzes conducted on synthetic databases in this study

546   using a roughness factor (J_2) demonstrate that at least 4% of the total observations should be fed

547   into the filter to ensure fluctuations are sufficiently reduced.

548   The results of this study show that SMA tends to considerably distort the underlying trend at a

549   bandwidth ratio of 0.10 (Fig. 8 and 9), and its lagged response with respect to real-time monitoring

550   is almost three times that of GWMA results. As a result, a bandwidth ratio between 0.04 and 0.07

551   is suggested. However, we caution that the bandwidth should be selected with complete

552   awareness that SMA is highly sensitive to bandwidth, and sensitivity analyses on bandwidth are

553   recommended when defining an EWS. Corresponding observations were made during the

554   analysis of displacement data from Geocubes installed on the Ten-mile landslide.

555   Error calculations show that GWMA and S-G outperform SMA in both direct and indirect filtration

556   and are more successful in preserving the true displacement trend. The near-zero lagged

557   response of S-G makes it a notable candidate for developing an EWS. Nonetheless, its intrinsic

558   shortcoming in handling peaks, leading to a pulsating effect, will pose challenges for its utilization.

559   The bandwidth range used for SMA is also suggested to be applied with the S-G filter.

560   GWMA results suggest a proper trade-off can be achieved between minimizing the lag time and

561   scatter and avoiding the pulsating effect. Compared to SMA and S-G, GWMA is less sensitive to

562   changes in the bandwidth. Analyses focused on the Geocube data also confirm that GWMA is

563   capable of constraining the fluctuations in the velocity diagram while not attenuating variations in

564   the displacement rate diagram. Moreover, the lag quantification chart proposed could reliably

565   capture the required shift with a greater degree of confidence in comparison to SMA even at the

566   largest bandwidth ratio studied here (0.10). The bandwidth for GWMA can therefore range from

567   0.04 to 0.10. Moreover, we observed consistency between direct and indirect filtration results

568   using GWMA but greater differences when using SMA or S-G results. This was especially the

569   case in the early parts of the datasets and at some locations where outlier elimination was likely

570   ineffective.

571   Filter and bandwidth selections should not be arbitrarily or purely empirical, as differences in

572   outcomes can be substantial. An automated surveillance system for landslides demands stability

573   in filter performance for a variety of circumstances, considering the ground can experience

574   irregular sequences of acceleration and deceleration. The results here suggest practice moves

575   away from the adoption of SMA due to the limitations discussed. S-G demonstrates some

576   inconsistent or erratic performance for certain displacement trends, which is detrimental although

577   overall the error is smaller than for SMA. On the balance of its strengths and limitations as

578   evaluated in this study, GWMA appears to be the more robust approach.

579   **6. Conclusions**

580   This study evaluated the suitability of SMA, GWMA, and S-G filters for scatter reduction of

581   datasets targeted for use in an EWS. A total of different 12 scenarios with harmonic and

582   instantaneous changes were synthetically generated and random variations with Gaussian

583   distribution were then added to produce unfiltered results. The three filters considered were then

584   each applied with different bandwidths and the error computed. These filters were also

585   successfully applied to the records from two Geocubes installed on the Ten-mile landslide. The

586   results led to the following conclusions:

587   • When used for direct filtration of harmonic scenarios, the error resulting from the GWMA

588   approach is approximately one-third that of the SMA approach. The S-G approach results

589   in near-zero error regardless of the values of the bandwidth ratio and n/t. When used for

590   direct filtration of instantaneous scenarios, the superiority of S-G is no longer unconditional

591   and depends on the bandwidth ratio; this reflects the fact that S-G cannot appropriately

592   handle peaks in the velocity diagram.

593   • When used for indirect filtration of harmonic scenarios, S-G again outperforms the other

594   methods. The error associated with GWMA is marginally less than for SMA. These

595   observations are not valid when the filters are applied to instantaneous scenarios, as

596   GWMA results in less error than S-G at bandwidth ratios above 0.03.

597   • Detailed investigations with scenarios 11 and 12 demonstrate that SMA distorts the

598   underlying trend by displacing and sometimes neglecting peak(s), while GWMA and S-G

599   tend to preserve them somewhat similarly.

600   • Due to the presence of negative weights in the S-G kernel, some artificial smaller troughs

601   and peaks are created after major peaks. This phenomenon, referred to herein as a

602   pulsating effect, results in an unfavorable performance of S-G on the velocity and

603   displacement diagrams, especially in the presence of outliers.

604   • Investigations on the roughness factor reveal the bandwidth ratio should be at least 0.04.

605   Taking this into account, GWMA seems to be the most reasonable option as the related

606   uncertainties are much smaller than for S-G and the error is acceptable and less than for

607   SMA.

608   • A consequence of using asymmetric windows in the filtering process is a lag in the SMA

609   and GWMA results that increases with increasing bandwidth ratio. Lag quantification

610   suggests a correlation between the needed shift and bandwidth ratio that can be used to

611   eliminate the lag. SMA requires approximately three times the shift of GWMA on average.

612   • Application of these filters to displacement data reported by Geocubes shows SMA and

613   S-G are unable to properly handle data points at the beginning of the dataset (i.e., near

614   the boundary) in indirect filtration of the velocity diagram. Moreover, SMA and S-G are

615   inclined to respectively underestimate and overestimate peaks and fluctuations in the

616   velocity diagram. Overall, GWMA provides the most reliable filtered values for velocity with

617   no distinct difference between direct and indirect filtration.

618 **Appendix A**

619 Consider a polynomial of degree k that is intended to be fitted over an odd number of points

620 denoted as z. The weighting coefficients of the Savitzky-Golay filter can be extracted from the first

621 row of matrix C (Eq. 7):

622
$$C = (J^T J)^{-1} J^T,$$
(7)

623 where T operator is the transpose of a matrix and J is the Vandermonde matrix, with elements at

624 the ith row and jth column ($1 \leq i \leq z$ and $1 \leq j \leq k+1$) that can be achieved as follows:

625
$$J_{ij} = m_i^{j-1},$$
(8)

626 where m is the local index of points ($-(z+1)/2 \leq m \leq (z+1)/2$). As an example, the kernel of an S-G

627 filter that fits a quadratic polynomial ($k=2$) over seven points ($z=7$) is attained here. In the first

628 step, J is set up as follows:

629
$$J = \begin{bmatrix} 1 & (-3)^1 & (-3)^2 \\ 1 & (-2)^1 & (-2)^2 \\ 1 & (-1)^1 & (-1)^2 \\ 1 & (0)^1 & (0)^2 \\ 1 & (1)^1 & (1)^2 \\ 1 & (2)^1 & (2)^2 \\ 1 & (3)^1 & (3)^2 \end{bmatrix}.$$
(9)

630 Then, using Eq. 1, matrix C is computed as Eq. 10:

631
$$C = \begin{bmatrix} -0.0952 & 0.1429 & 0.2857 & 0.3333 & 0.2857 & 0.1429 & -0.0952 \\ -0.1070 & -0.0714 & -0.0357 & 0 & 0.0357 & 0.0714 & 0.1071 \\ -0.0595 & 0 & -0.0357 & -0.0476 & -0.0357 & 0 & 0.0595 \end{bmatrix}.$$
(10)

632 The second and third rows of C are the coefficients to find the filtered values' first and second

633 derivations at the point of interest, respectively.

634 **Data availability**

635 The synthetic database can be generated through the comprehensive steps provided here. The

636 Geocube measurements of the Ten-mile landslide displacement are not publicly available.

Author contribution

Sohrab Sharifi: conceptualization, methodology, analysis, writing – draft preparation. Michael Hendry: supervision, review, writing – review and editing, project administration. Renato Macciotta: supervision, review, writing – review and editing. Trevor Evans: writing – review and editing, validation, project administration.

Competing interests

The authors declare that they have no conflict of interest.

Acknowledgment

The authors thank Canadian National Railway (CN) for providing access to the Ten-mile site and for purchasing the Geocube units. This research was conducted through the (Canadian) Railway Ground Hazard Research Program, which is funded by the Natural Sciences and Engineering Research Council of Canada (NSERC ALLRP 549684-19), Canadian Pacific Railway, CN, and Transport Canada.

References

Atzeni, C., Barla, M., Pieraccini, M., and Antolini, F.: Early warning monitoring of natural and engineered slopes with ground-based synthetic-aperture radar, Rock Mech. Rock Eng., 48(1), 235-246, https://doi.org/10.1007/s00603-014-0554-4, 2015.

Benoit, L., Briole, P., Martin, O., and Thom, C.: Real-time deformation monitoring by a wireless network of a low-cost GPS, J. Appl. Geodesy, 8(2), 119-128, 2014.

Benoit, L., Briole, P., Martin, O., Thom, C., Malet, J. P., and Ulrich, P.: Monitoring landslide displacements with the Geocube wireless network of low-cost GPS, Eng. Geol., 195, 111-121, 2015.

659 BGC Engineering Inc. CN Lillooet Sub. M. 167.7 (Fountain Slide) September 2015 Drilling and

660 Instrumentation. Project report to Canadian National Railway, 2015.

661 BGC Engineering Inc. CN Lillooet Sub. M. 167.7 (Ten Mile Slide) April 2016 Drilling and

662 Instrumentation. Project report to Canadian National Railway, 2016.

663 Bovis, M. J.: Earthflows in the interior plateau, southwest British Columbia, Can. Geotech. J.,

664 22(3), 313-334, 1985.

665 Bozzano, F., Mazzanti, P., and Moretto, S.: Discussion to: 'Guidelines on the use of inverse

666 velocity method as a tool for setting alarm thresholds and forecasting landslides and structure

667 collapses' by T. Carlà, E. Intrieri, F. Di Traglia, T. Nolesini, G. Gigli, and N.

668 Casagli, Landslides, 15(7), 1437-1441, 2018.

669 Carlà, T., Farina, P., Intrieri, E., Botsialas, K., and Casagli, N.: On the monitoring and early-

670 warning of brittle slope failures in hard rock masses: Examples from an open-pit mine, Eng.

671 Geol., 228, 71-81, 2017a.

672 Carlà, T., Intrieri, E., Di Traglia, F., Nolesini, T., Gigli, G., and Casagli, N.: Guidelines on the use

673 of inverse velocity method as a tool for setting alarm thresholds and forecasting landslides and

674 structure collapses, Landslides 14(2), 517-534, 2017b.

675 Carlà, T., Macciotta, R., Hendry, M., Martin, D., Edwards, T., Evans, T., Farina, P., Intrieri, E., and

676 Casagli, N.: Displacement of a landslide retaining wall and application of an enhanced failure

677 forecasting approach, Landslides, 15(3), 489-505, 2018.

678 Carlà, T., Intrieri, E., Raspini, F., Bardi, F., Farina, P., Ferretti, A., Colombo, D., Novali, F., and

679 Casagli, N.: Perspectives on the prediction of catastrophic slope failures from satellite InSAR, Sci.

680 Rep., 9(1), 1-9, 2019.

681 Carri, A., Valletta, A., Cavalca, E., Savi, R. and Segalini, A.: Advantages of IoT-based

682 geotechnical monitoring systems integrating automatic procedures for data acquisition and

683 elaboration, Sensors, 21(6), 2249, 2021.

684 Casagli, N., Frodella, W., Morelli, S., Tofani, V., Ciampalini, A., Intrieri, E., Raspini, F., Rossi, G.,

685 Tanteri, L., and Lu, P.: Spaceborne, UAV and ground-based remote sensing techniques for

686 landslide mapping, monitoring and early warning, Geoenviron. Disasters, 4(1), 1-23, 2017.

687 Chae, B. G., Park, H. J., Catani, F., Simoni, A., and Berti, M.: Landslide prediction, monitoring

688 and early warning: a concise review of state-of-the-art, Geosci. J., 21(6), 1033-1070, 2017.

689 Chen, M., and Jiang, Q.: An early warning system integrating time-of-failure analysis and alert

690 procedure for slope failures, Eng. Geol., 272, 105629, 2020.

691 Clague, J. J., and Bobrowsky, P. T.: International year of planet earth 8. Natural hazards in

692 Canada, Geosci. Can. 37(1), 17-37, 2010.

693 Cleveland, W. S.: LOWESS: A program for smoothing scatterplots by robust locally weighted

694 regression, Am. Stat., 35(1), 54, 1981.

695 Cleveland, W. S., and Devlin, S. J.: Locally weighted regression: an approach analysis by local

696 fitting, J. Am. Stat. Assoc. 83(403), 596-610, 1988.

697 Clifford, P.: Monte Carlo methods, in: statistical methods for Physical Science, edited by: Stanford,

698 J. L., and Vardeman, S. B., Elsevier, 125-153, 1994.

699 Davies, L., and Gather, U.: The identification of multiple outliers, J. Am. Stat. Assoc., 88(423),

700 782-792, 1993.

701 Deane, E.: The Application of Emerging Monitoring Technologies on Very Slow Vegetated

702 Landslides, Dissertation, University of Alberta, 2020.

703 Desrues, M., Malet, J.P., Brenguier, O., Carrier, A., Mathy, A., and Lorier, L.: Landslide kinematics

704 inferred from in situ measurements: the Cliets rock-slide (Savoie, French Alps), Landslides, 1-16,

705 2021.

706 Dick, G.J., Eberhardt, E., Cabrejo-Liévano, A.G., Stead, D. and Rose, N.D.: Development of an

707 early-warning time-of-failure analysis methodology for open-pit mine slopes utilizing ground-

708 based slope stability radar monitoring data, Canadian Geotechnical Journal, *52*(4), 515-529,

709 2015.

710 Donati, D., Stead, D., Lato, M., and Gaib, S.: Spatio-temporal characterization of slope damage:

711 insights from the Ten Mile Slide, British Columbia, Canada, Landslides, 17(5), 1037-1049, 2020.

712 Dorberstein, D.: Fundamentals of GPS Receivers: A Hardware Approach, Springer Science &

713 Business Media, Nipomo, CA, USA, 2011.

714 Gaib, S., Wilson, B., and Lapointe, E.: Design, construction and monitoring of a test section for

715 the stabilization of an active slide area utilizing soil mixed shear keys installed using cutter soil

716 mixing, Proceedings of the ISSMGE - TC 211 International Symposium on Ground Improvement

717 IS-GI, Brussels, 3, 147-158, 2012.

718 Grebby, S., Sowter, A., Gluyas, J., Toll, D., Gee, D., Athab, A., and Girindran, R.: Advanced

719 analysis of satellite data reveals ground deformation precursors to the Brumadinho Tailings Dam

720 collapse, Communications Earth & Environment, 2(1), 1-9, 2021.

721 Guthrie, R. H.: Socio-Economic Significance: Canadian Technical Guidelines and Best Practices

722 Related to Landslides: A National Initiative for Loss Reduction, Natural Resources Canada,

723 Ottawa, ON, 2013.

724 Hampel, F. R.: A general qualitative definition of robustness, Ann. Math. Stats., 42(6), 1887-1896,

725 1971.

726   Hongtao, N.: Smart safety early warning model of landslide geological hazard based on BP neural

727   network, Safety Sci., 123, 104572, 2020.

728   Huntley, D., Bobrowsky, P., Charbonneau, F., Journault, J., Macciotta, R., and Hendry, M.:

729   Innovative landslide change detection monitoring: application of space-borne InSAR techniques

730   in the Thompson River valley, British Columbia, Canada, Workshop on World Landslide Forum

731   3, 219-229, 2017.

732   Intrieri, E., Gigli, G., Mugnai, F., Fanti, R., and Casagli, N.: Design and implementation of a

733   landslide early warning system, Eng. Geol., 147, 124-136, 2012.

734   Intrieri, E., Raspini, F., Fumagalli, A., Lu, P., Del Conte, S., Farina, P., Allievi, J., Ferretti, A., and

735   Casagli, N.: The Maoxian landslide as seen from space: detecting precursors of failure with

736   Sentinel-1 data, Landslides, 15(1), 123-133, 2018.

737   Journault, J., Macciotta, R., Hendry, M. T., Charbonneau, F., Huntley, D., and Bobrowsky, P. T.:

738   Measuring displacements of the Thompson River valley landslides, south of Ashcroft, BC,

739   Canada, using satellite InSAR, Landslides, 15(4), 621-636, 2018.

740   Karl, J. H.: Introduction to Digital Signal Processing, Academic Press, San Diego, 1989.

741   Kothari, U.C. and Momayez, M.: New approaches to monitoring, analyzing and predicting slope

742   instabilities, Journal of Geology and Mining Research, 10(1), 1-14, 2018.

743   Lacasse, S., and Nadim, F.: Landslide risk assessment and mitigation strategy, in: Landslides–

744   Disaster Risk Reduction, edited by: Sassa, K., and Canuti, P., Springer, 31-61, 2009.

745   Leroueil, S.: Natural slopes and cuts: movement and failure mechanisms, Géotechnique, 51(3),

746   197-243, 2001.

747   Liu, H., Shah, S., and Jiang, W.: On-line outlier detection and data cleaning, Comput. Chem. Eng.,

748   28(9), 1635-1647, 2004.

749   Macciotta, R., and Hendry, M. T. Remote sensing applications for landslide monitoring and

750   investigation in western Canada, Remote Sens., 13(3), 366-389, 2021.

751   Macciotta, R., Hendry, M., and Martin, C. D.: Developing an early warning system for a very slow

752   landslide based on displacement monitoring, Nat. Hazards, 81(2), 887-907, 2016.

753   Macciotta, R., Carlà, T., Hendry, M., Evans, T., Edwards, T., Farina, P., and Casagli, N.: The 10-

754   mile Slide and response of a retaining wall to its continuous deformation, Workshop on World

755   Landslide Forum, 553-562, 2017a.

756   Macciotta, R., Rodriguez, J., Hendry, M., Martin, C. D., Edwards, T., and Evans, T.: The 10-mile

757   Slide north of Lillooet, British Columbia–history, characteristics, and monitoring. In Proceedings,

758   3rd North American Symposium on Landslides, 937-948, 2017b.

759   Pearson, R. K.: Outliers in process modeling and identification, IEEE Trans. Control Syst.

760   Technol., 10(1), 55-63, 2002.

761   Reid, M. E., Godt, J. W., LaHusen, R. G., Slaughter, S. L., Badger, T. C., Collins, B. D., Schulz,

762   W. H., Baum, R. L., Coe, J. A., Harp, E. L. and Schmidt, K. M.: When hazard avoidance is not an

763   option: lessons learned from monitoring the postdisaster Oso landslide, USA, Landslides, 18,

764   2993-3009, 2021.

765   Rodriguez, J. L., Macciotta, R., Hendry, M., Edwards, T., and Evans, T.: Slope hazards and risk

766   engineering in the Canadian railway network through the Cordillera, Proceedings of the AIIT

767   International Congress on Transport Infrastructure and Systems (TIS 2017), Rome, Italy, 163-

768   168, 2017.

769   Rodriguez, J., Hendry, M., Macciotta, R., and Evans, T.: Cost-effective landslide monitoring GPS

770   system: characteristics, implementation, and results, Geohazards7, Canmore, Alberta, 2018.

771   Rodriguez, J., Macciotta, R., Hendry, M. T., Roustaei, M., Gräpel, C., and Skirrow, R.: UAVs for

772   monitoring, investigation, and mitigation design of a rock slope with multiple failure mechanisms—

773   a case study, Landslides, 17, 2027-2040, 2020.

774   Rousseeuw, P. J., and Hubert, M.: Robust statistics for outlier detection. Wiley Interdiscip. Rev.

775   Data Min. Knowl. Discov., 1(1), 73-79, 2011.

776   Salgado, C. M., Azevodo, C., Proença, H., and Vieira, S. M.: Noise versus outliers. In: Secondary

777   Analysis of Electronic Health Records, MIT Critical Data, Springer, 163-183, 2016.

778   Savitzky, A., and Golay, M. J.: Smoothing and differentiation of data by simplified least squares

779   procedures, Anal. Chem., 36(8), 1627-1639, 1964.

780   Schafer, M. B.: Kinematics and Controlling Mechanics of Slow-moving Ripley Landslide.

781   Dissertation, University of Alberta, 2016.

782   Schafer, R. W.: What is a Savitzky-Golay filter? [lecture notes], IEEE Signal Process. Mag., 28(4),

783   111-117, 2011.

784   Scoppettuolo, M.R., Cascini, L., and Babilio, E.: Typical displacement behaviours of slope

785   movements, Landslides, 17, 1105-1116. 2020

786   Smith, S.: Digital Signal Processing: A Practical Guide for Engineers and Scientists, Elsevier,

787   2013.

788   Thiebes, B., Bell, R., Glade, T., Jäger, S., Mayer, J., Anderson, M., and Holcombe, L.: Integration

789   of a limit-equilibrium model into a landslide early warning system, Landslides, 11(5), 859-875,

790   2014.

791   Tofani, V., Rasipini, F., Catani, F., and Casagli, N.: Persistent Scatterer Interferometry (PSI)

792   technique for landslide characterization and monitoring, Remote Sens., 5(3), 1045-1065, 2013.

793 UNISDR: United Nations International Strategy for Disaster Reduction: Terminology on Disaster

794 Risk Reduction, 2009. Available at http://www.unisdr.org.

795 Vaziri, A., Moore, L., and Ali, H.: Monitoring systems for warning impending failures in slopes and

796 open pit mines, Nat. Hazards, 55(2), 501-512, 2010.

797 Wang, G.: GPS landslide monitoring: single base vs. network solutions-a case study based on

798 the Puerto Rico and Virgin Islands permanent GPS network, J. Geodet. Sci., 1(3), 191-203, 2011.

799 William, S. C.: Robust locally weighted regression and smoothing scatterplots. J. Am. Stat.

800 Assoc., 74(368), 829-836, 1979.

801 Woods, A., Hendry, M. T., Macciotta, R., Stewart, T., and Marsh, J.: GB-InSAR monitoring of

802 vegetated and snow-covered slopes in remote mountainous environments, Landslides, 17, 1713-

803 1726, 2020.

804 Woods, A., Macciotta, R., Hendry, M. T., Stewart, T., and Marsh, J.: Updated understanding of

805 the deformation characteristics of the Checkerboard Creek rock slope through GB-InSAR

806 monitoring, Eng. Geol., 281, 105974, 2021.

807 Yao, Z., Xie, J., Tian, Y., and Huang, Q.: Using Hampel identifier to eliminate profile-isolated

808 outliers in laser vision measurement, J. Sens., 2019, 3823691, 2019.

809 Yin, Y., Wang, H., Gao, Y., and Li, X.: Real-time monitoring and early warning of landslides at

810 relocated Wushan Tow, the Three Gorges Reservoir, China, Landslides, 7(3), 339-349, 2010.

811 Zhang, Y.H., Ma, H.T. and Yu, Z.X.: Application of the method for prediction of the failure location

812 and time based on monitoring of a slope using synthetic aperture radar, Environ. Earth Sci.,

813 80(21) 1-13, 2021a.

814 Zhang, Y. G., Tang, J., He, Z. Y., Tan, J., and Li, C.: A novel displacement prediction method

815 using gated recurrent unit model with time series analysis in the Erdaohe landslide. Nat. Hazards,

816 105, 783-813, 2021b.

817   Zhou, X.P., Liu, L.J., and Xu, C.: A modified inverse-velocity method for predicting the failure time

818   of landslides, Eng. Geol., 268, 105521, 2020.

819   Zimek, A., and Filzmoser, P.: There and back again: Outlier detection between statistical

820   reasoning and data mining algorithms, Data Min. Knowl. Discov., 8(6), 1280, 2018.

821